Monthly Notices of the Royal Astronomical Society, Volume 515, Issue 1, September 2022, pp. 451–472
DOI: 10.1093/mnras/stac1741

On High-Order Numerical Schemes for Viscous Relativistic Hydrodynamics through the Kelvin–Helmholtz Instability

Jamie F. Townsend,[1,2]★ Shu-ichiro Inutsuka,[2] László Könözsy,[1] and Karl W. Jenkins[1]
[1]*Centre for Computational Engineering Sciences, Cranfield University, Cranfield, MK43 0AL, UK*
[2]*Department of Physics, Nagoya University, Nagoya, 464-8602, Japan*

ABSTRACT
This work assesses the dissipative properties of high-order numerical methods for relativistic hydrodynamics (RHD). A causal theory of physical dissipation is included within a finite volume High-Resolution Shock-Capturing (HRSC) framework based on the Israel–Stewart theory to study high-order WENO (Weighted-Essentially Non-Oscillatory) schemes for simulating the relativistic Kelvin–Helmholtz instability. We provide an estimation of the numerical dissipation of high-order schemes based on results obtained both with and without physically resolved dissipation and determine an empirical relationship between the numerical dissipation and the grid resolution. We consider the appearance of secondary flow features within the evolution of the Kelvin–Helmholtz instability and determine that they are numerical artifacts—this is partly based on arguments presented in terms of a frame-dependent form of the relativistic Reynolds number. There is a potential advantage of using high-order schemes in terms of their accuracy and computational cost on coarser grid resolutions when directly compared to low-order schemes on a fine grid in the presence of physical viscosity. It is possible to find reasonable agreement between numerical results that employ lower-order schemes using a finer grid resolution and results that employ higher order schemes at a coarser grid resolution when sufficient viscosity is present. Overall, the present analysis gives an insight into the numerical dissipation of high-order shock-wave capturing schemes which can be relevant to computational studies of astrophysical phenomena in the relativistic regime. The results presented herein are problem and scheme-dependent and serve to highlight the different roles of numerical and physical dissipation.

Key words: hydrodynamics – relativistic processes – instabilities – methods: numerical

1 INTRODUCTION

Relativistic flows are supposed to play crucial roles in a number of high-energy astrophysical phenomena such as relativistic jets, gamma-ray bursts, pulsar winds, accretion flows around compact objects, and core-collapse supernovae. Among them, the recent detection of the binary neutron-star (BNS) merger event, GW170817 (Abbott et al. 2017a), stimulated extensive research on relativistic hydrodynamics (RHD) and relativistic magnetohydrodynamics (RMHD) in the context of a short gamma-ray burst (Abbott et al. 2017b) and of a kilonova (Drout et al. 2017; Cowperthwaite et al. 2017). BNS mergers are highly dynamical and nonlinear phenomena and the emergence of turbulence and the dissipation due to viscosity are also discussed (Baiotti & Rezzolla 2017; Siegel et al. 2013; Kiuchi et al. 2018), which provides a challenge for numerical simulations.

Modern-day RHD and RMHD numerical solvers often make use of the High-Resolution Shock-Capturing (HRSC) framework. This encompasses the Godunov-type philosophy of a numerical flux computation at each cell interface which is typically overcome using an approximate Riemann solver. This strategy has proved highly effective for RHD and RMHD applications where strong shock waves are encountered and represents the current standard for grid-based methods in this field. High-order numerical methods such as the Weighted Essentially Non-Oscillatory (WENO) approach have found increasing use within RHD since they show promising numerical solutions to systems of hyperbolic conservation laws (Nunez-de la Rosa & Munz 2016). For the sake of clarity, a high-order scheme in the present work is defined as those with an order of accuracy of three or above and we refer strictly to high-order spatial reconstruction, which is used to acquire the initial conditions for the local Riemann problem. The increasing demand placed on the computational physics community for high-fidelity numerical simulations requires consideration of the computational power and available memory as a parameter of efficacy which may encumber numerical simulations. It is well-known that second-order accurate schemes, which are simple and robust, at sufficiently high resolutions are capable of reproducing solutions with an error as

★ E-mail: j.townsend@cranfield.ac.uk (JFT)

small as desired and that all methods become first-order accurate near discontinuities (Rezzolla & Zanotti 2013). On the other hand, high-order schemes are often surrounded with the idea that they are complex and therefore troublesome to implement, less robust, and computational more expensive when used at the same resolution as their lower-order counterparts. Shu (2003) showed that the use of high-order schemes can actually reduce computational cost as their deployment on a lower resolution grid can yield results competitive with a low-order scheme on a finer gird. Computational Fluid Dynamics (CFD) simulations within the aerospace community regularly adopt high-order numerical schemes that strive to resolve complex turbulent flow physics, see e.g. Ricci et al. (2020). For flows containing a range of length-scales, the use of high-order methods may then prove extremely powerful for astrophysical events containing some form of shock–turbulence interaction (Abdikamalov et al. 2016). To-date, RHD and RMHD simulations are often restricted to inviscid (perfect) fluids such that heat conduction, viscosity, and magnetic resistivity are neglected. For the vast majority of astrophysical applications wherein the typical time and length-scales are very large compared to the fluid time-scale, the assumption is justified.

Early motivation for the inclusion of physical viscosity within RHD simulations largely resides in its necessity for the study of the quark–gluon plasma (QGP) created through the collision of heavy ions, see Romatschke (2010) for an overview of the subject. There is however a recent surge in interest surrounding dissipative effects within the astrophysics community for the study of BNS merger events and black hole accretion (Chandra et al. 2015). As recently described by Chabanov et al. (2021), BNS merger events may require a description of bulk viscosity to correctly understand the emitted gravitational-wave signal. Moreover, as demonstrated by Baiotti et al. (2009), magnetic and fluid instabilities such as the Kelvin–Helmholtz instability can also develop in this process, which will inevitably result in turbulent flow. Turbulence is a research topic in its infancy within the context of numerical relativity and requires a consistent description of physical viscosity for its fundamental study, see e.g. Mignone et al. (2009), Zhang et al. (2009), Beckwith & Stone (2011), Radice & Rezzolla (2012), Zrake & MacFadyen (2013), Radice & Rezzolla (2013).

The Kelvin–Helmholtz instability occurs due to velocity shear within a continuous fluid or across an interface separating two different fluids. This instability may occur within astrophysical environments as well as terrestrial engineering applications, see e.g. Rana et al. (2011). The shear leads to vorticity development which grows with time and subsequently invokes turbulence. Not only is this test case used as a means to evaluate the performance of numerical methods, it is also studied in itself within the context of relativistic fluid flow. Martí et al. (1997) demonstrate through numerical simulations that relativistic jets were stable due to the suppression of the Kelvin–Helmholtz instability at high-enough Lorentz factors, confirming the analysis by Ferrari et al. (1978). Okamoto & Nonaka (2017) discuss the possible development of the Kelvin–Helmholtz instability during relativistic heavy-ion collisions and indicate that a numerical code with a lower numerical viscosity is required for its study and Mourão Roque & Lugones (2018), in a similar spirit, under conditions applicable to the early evolution of the universe, assessed the role of the instability at the QCD epoch. Using RMHD, Bucciantini & Del Zanna (2006) investigated the development of the instability under conditions representative of a Pulsar Wind Nebulae environment. An investigation is also conducted by Bodo et al. (2004) who determine analytical expressions for the dispersion relation when an appropriate reference frame is used. Parametric studies by Tian & Chen (2016) using non-relativistic MHD to compare the dependencies of various physical parameters, such as viscosity, show how its evolution changes in the context of astrophysical applications.

The most popular choice of dissipative theory within numerical relativity is attributed to Israel & Stewart (1979) and commonly referred to as Israel–Stewart theory throughout the literature. Authors such as Baier & Romatschke (2007) relied on a central difference method and Schenke et al. (2011) incorporated Israel–Stewart theory in a second-order accurate Riemann solver-free framework using the Kurganov and Tadmor (KT) central scheme, they note that negative values of the rest-mass density sometimes plague their numerical simulations (Schenke et al. 2010). Roy & Chaudhuri (2012) employed the SHASTA scheme developed by Boris & Book (1973) which utilizes the concept of flux-corrected transport (FCT) and again makes no use of a Riemann solver. While these numerical solvers were able to fathom information of interest regarding the QGP, the conservative and shock-capturing properties within the numerical framework could have been improved if HRSC numerical schemes were employed. Due to the success of Godunov-type methods applied to inviscid RHD, a numerical methodology was sought in which its advantages could be applied for the incorporation of physical dissipation. This is not an entirely straightforward task because HRSC methods rely on the hyperbolicity of the conservation equations such that the conserved variables are evolved in time according to the spatial fluxes. Including a causal theory of physical dissipation such as Israel–Stewart theory disrupts this methodology because the dissipative variables must also be evolved in time according to a relaxation timescale which is typically much shorter than the hydrodynamic timescale. To circumvent this issue, Takamoto & Inutsuka (2011) proposed splitting the governing equations into a dissipative and non-dissipative part; this practice meant that HRSC developments could be exploited. Authors such as Karpenko et al. (2014), Akamatsu et al. (2014), and Okamoto et al. (2016) also adopted this strategy in their numerical solvers tailored to study the QGP via the use of a Milne coordinate system. Del Zanna et al. (2013) also make use of the HRSC finite difference framework by applying a higher-order scheme to the fluxes themselves without splitting the governing equations into a perfect/non-perfect part.

Numerical errors are often associated with either numerical dispersion or numerical viscosity (dissipation). Numerical dispersion contributes to phase errors in the solution whilst the latter acts to smooth-out flow features via smearing—in this study only numerical viscosity is considered. An analogy between physical and numerical viscosity is often made as they can have a similar effect on the solution. Numerical viscosity is required to maintain a stable solution, a lack of which may result in issues such as the so-called Carbuncle problem (Townsend et al. 2020). However, if the manifest numerical viscosity is too large, this can have a negative impact on solution fidelity and small-scale flow features may be unwittingly removed. The numerical viscosity present within a numerical scheme was considered by Beckwith & Stone (2011) and Radice & Rezzolla (2012) using their simulations of the relativistic Kelvin–Helmholtz instability by employing the rest-mass density power spectrum to quantify the power residing at small-scales. Within their investigations, secondary flow features were present when higher-fidelity methods were used that are claimed to be non-physical and purely numerical in nature. Similarly for the non-relativistic case, San & Kara (2015) also reported the energy power spectrum for the same reason as well as tracking the evolution of the kinetic energy over time, enabling quantitative insight into the dissipative proper-

ties of the numerical schemes employed. Tsoutsanis et al. (2015) were able to isolate the energy losses arising from numerical and physical viscosity for the numerical solution of the non-relativistic Navier–Stokes equations applied to the two-dimensional vortex-pairing problem. Numerical viscosity measurements were thus not attainable *a priori* which led Rembiasz et al. (2017) to seek a general formula capable of estimating the numerical viscosity (and resistivity in their case) based on knowledge of the numerical schemes and grid resolution. This fared well during the 1D and 2D simulations in their work. More recently, Obergaulinger & Aloy (2020) sought to determine the rates of numerical dissipation for the non-relativistic Kelvin–Helmholtz instability by analysis of the instability growth for simulations with only numerical viscosity present and those with a finite viscosity. They were able to determine a relationship in terms of the instability growth-rate that led to an expression capable of estimating the numerical viscosity contained within the solutions.

This work investigates the dissipative properties of three flavors of high-order WENO spatial reconstruction scheme that have witnessed increasing use within the RHD and RMHD community for astrophysical applications. The relativistic Kelvin–Helmholtz instability is used as a test case hence we are not investigating the diffusive nature of the schemes in the presence of shock waves. Instead, we aim to provide an estimation of the inherent numerical viscosity present when high-order spatial reconstruction is employed and evaluate the performance of these schemes in the presence of physically resolved viscosity.

2 GOVERNING EQUATIONS

This investigation requires the numerical solution of the RHD equations when physical dissipation is resolved. Throughout this work we use natural units ($c = 1$) and a Cartesian coordinate system where the Minkowski metric tensor is given by $g_{\mu\nu} = \mathrm{diag}(-,+,+,+)$. Greek letters take values from 0 to 3 whereas Roman letters span values 1 to 3 with the definition $(0,1,2,3) \equiv (t,x,y,z)$. We refer to an inviscid fluid as perfect and a dissipative/viscous fluid as non-perfect. The term ideal refers only to the equation of state (EOS).

The governing equations of RHD are formulated as a system of conservation laws,

$$\nabla_\mu N^\mu = 0, \tag{1a}$$

$$\nabla_\mu T^{\mu\nu} = 0, \tag{1b}$$

corresponding to the conservation of particle number, and momentum and energy, respectively. N^μ is the particle number density current and $T^{\mu\nu}$ denotes the energy–momentum tensor. By defining a set of conserved variables the equations are easily cast into conservation-law form, such that we have a system according to Banyuls et al. (1997),

$$\frac{\partial}{\partial t}\boldsymbol{U} + \frac{\partial}{\partial x}\boldsymbol{F}(\boldsymbol{U}) + \frac{\partial}{\partial y}\boldsymbol{G}(\boldsymbol{U}) + \frac{\partial}{\partial z}\boldsymbol{H}(\boldsymbol{U}) = 0, \tag{2}$$

where the vector $\boldsymbol{U}$ is a vector of conserved variables and $\boldsymbol{F}$, $\boldsymbol{G}$, and $\boldsymbol{H}$ are flux vectors in the x-, y-, and z-direction, respectively. This formulation lends itself well to powerful numerical methodologies that enable accurate and robust shock-capturing practices.

2.1 Inviscid RHD

The perfect fluid approximation of RHD neglects contributions from dissipative phenomena such as viscosity and thermal conductivity. For a perfect fluid, the particle number density current N^μ and energy–momentum tensor $T^{\mu\nu}$ are given by

$$N^\mu = nu^\mu, \tag{3a}$$

$$T^{\mu\nu} = \rho h u^\mu u^\nu + p g^{\mu\nu}, \tag{3b}$$

where n is the proper particle number density, u^μ is the fluid four-velocity that satisfies the condition $u^\mu u_\mu = -1$, p is the fluid pressure, and ρ is the rest-mass density. In this work an ideal fluid is assumed, meaning that an EOS corresponding to an ideal gas of the form $p = p(\rho,\epsilon)$ is used throughout, where ϵ denotes the specific internal energy of the fluid. The equation of state and specific enthalpy h are given by,

$$p = \rho\epsilon(\Gamma - 1), \tag{4}$$

and,

$$h = 1 + \frac{\Gamma}{\Gamma - 1}\frac{p}{\rho}, \tag{5}$$

respectively. The constant adiabatic index Γ used herein represents the ratio of specific heats and is chosen as $\Gamma = 4/3$ throughout the present study. The relativistic speed of sound c_s is consequently expressed as,

$$c_s^2 = \frac{\Gamma p}{\rho h}. \tag{6}$$

The conserved variables for the conservation of mass D, momentum S^i, and energy E are given by,

$$\boldsymbol{U} = \begin{bmatrix} D \\ S^i \\ E \end{bmatrix} = \begin{bmatrix} \rho W \\ \rho h W^2 u^i \\ \rho h W^2 - p \end{bmatrix}, \tag{7}$$

where $u^i \equiv (u^x, u^y, u^z)$ is the fluid three-velocity and the Lorentz factor W is defined as,

$$W = \frac{1}{\sqrt{1 - u^i u_i}}, \tag{8}$$

wherein the fluid four-velocity can be expressed as $u^\mu = W(1, u^i)$. The conservation laws provided by Eq. (1) written in the conservative form given by Eq. (2) are found to be,

$$\frac{\partial}{\partial t}\begin{pmatrix} D \\ S^i \\ E - D \end{pmatrix} + \frac{\partial}{\partial x^j}\begin{pmatrix} Du^j \\ S^i u^j + pI^{ij} \\ S^i - Du^j \end{pmatrix} = 0. \tag{9}$$

Note that we have adopted the practice of subtracting the rest-mass term from the energy term and similarly the mass flux with the energy flux. This practice is purely numerical and through extensive numerical testing it was found that this modification provided the most accurate solutions. We note that this is not a general statement as many authors have achieved accurate solutions using HRSC methods for RHD without this modification to the energy terms, see e.g. Nunez-de la Rosa & Munz (2016).

The eigenvalues for the system of conservation laws given in Eq. (9) in the x-direction are (Martí & Müller 2015),

$$\lambda_0 = u^i \quad \text{(triple)}, \tag{10a}$$

$$\lambda_\pm = \frac{1}{1 - u^i u_i c_s^2}\Bigg\{ u^x\left(1 - c_s^2\right) \pm c_s\sqrt{\left(1 - u^i u_i\right)\left[1 - u^x u^x - \left(u^i u_i - u^x u^x\right)c_s^2\right]}\Bigg\}. \tag{10b}$$

The eigenvalues are all real and distinct, thus implying that the

system of governing equations for a perfect relativistic fluid is hyperbolic. Symmetry considerations yield the corresponding eigenvalues in the y- and z-directions. The eigenvalues in Eq. (10) correspond to the wave speeds within the system and the maximum velocities permissible.

2.2 Dissipative RHD

Including physical dissipation within the relativistic framework first requires a renewed definition of the fluid four-velocity, u^μ. No special definition is needed for a perfect fluid where, by definition, no energy or particle flow can exist in the fluid rest (or co-moving) frame. Unlike the perfect fluid approximation however, both energy and particle diffusion are present hence the definition of a local rest frame becomes ambiguous. Additionally, the rest-mass density current N^μ, the energy–momentum tensor $T^{\mu\nu}$, and the entropy current $\mathcal{S}^\mu$ are considered to be primary field variables with no *a priori* relation to the four-velocity or any rest frame. Therefore, two physical perspectives are commonly used to define the fluid four-velocity. The so-called Landau frame in which the four-velocity is specified as having the same direction, since the energy flux vector allows for particle diffusion but not energy diffusion in the local rest frame (Landau & Lifshitz 1987). On the other hand the so-called Eckart frame can be used as the local rest-frame in which the four-velocity u^μ is defined to be parallel to the particle flux vector, meaning there is no particle diffusion and therefore the rest-mass density current remains unchanged and energy diffusion is present (Eckart 1940). In practice, however, it can be shown that the resolved physics is the same despite the choice of local rest-frame as demonstrated by Akamatsu et al. (2014) who showed that the particle diffusion in the Landau frame is equivalent to the heat diffusion in the Eckart frame.

Using the Eckart decomposition, the particle number density current N^μ and energy–momentum tensor $T^{\mu\nu}$ are written as,

$$N^\mu = nu^\mu, \tag{11a}$$

$$T^{\mu\nu} = \rho h u^\mu u^\nu + p g^{\mu\nu} + q^\mu u^\nu + q^\nu u^\mu + \tau^{\mu\nu}, \tag{11b}$$

where q^μ is the heat-flux vector and $\tau^{\mu\nu}$ is the viscosity tensor granting contributions from dissipative phenomena. The viscous tensor $\tau^{\mu\nu}$ is decomposed into contributions arising from shear and bulk viscosity related to the traceless and trace part of the viscosity tensor,

$$\tau^{\mu\nu} \equiv \Pi \gamma^{\mu\nu} + \pi^{\mu\nu}, \tag{12}$$

where $\gamma^{\mu\nu} \equiv g^{\mu\nu} + u^\mu u^\nu$ is the projection operator that projects any tensor on the hypersurface normal to u^μ and Π and $\pi^{\mu\nu}$ denotes the bulk viscosity and shear viscosity tensor, respectively.

The conservation laws in Eq. (1) are reformulated using the particle number density current N^μ and energy–momentum tensor $T^{\mu\nu}$ in Eq. (11) such that for non-perfect RHD we have,

$$\frac{\partial}{\partial t}\begin{pmatrix} D \\ S^i + q^0 u^i + q^i u^0 + \tau^{0i} \\ E - D + 2q^0 u^0 + \tau^{00} \end{pmatrix} + \frac{\partial}{\partial x^j}\begin{pmatrix} Du^i \\ S^i u^j + pI^{ij} + q^i u^j + q^j u^i + \tau^{ij} \\ S^j - Du^j + q^0 u^j + q^j u^0 + \tau^{0j} \end{pmatrix} = 0. \tag{13}$$

Eq. (13) provides the fundamental governing equations for non-perfect RHD in the presence of special relativity. While this system of equations is sound, definitions for the bulk viscosity Π, heat-flux vector q^μ and shear viscosity tensor $\pi^{\mu\nu}$ are still needed.

The second law of thermodynamics states that the change in entropy of a closed thermodynamic system will always be positive or zero. Hence the entropy production rate is,

$$\nabla_\mu \mathcal{S}^\mu \geq 0, \tag{14}$$

where $\mathcal{S}^\mu$ is the entropy four-vector which, along with N^μ and $T^{\mu\nu}$, comprise the state variables of the system for a non-perfect fluid. In the case of a perfect fluid the entropy current is defined as $\mathcal{S}^\mu = s\rho u^\mu$. According to Eckart (1940), for the entropy production rate to remain non-zero an additional contribution is required such that,

$$\mathcal{S}^\mu = s\rho u^\mu + \frac{R^\mu}{T} \tag{15}$$

where T is the temperature and R^μ is some four-vector with non-zero divergence and is assumed to be a function of the dissipative fluxes $\Pi, \pi^{\mu\nu}, q^\mu$, which vanish under the perfect fluid approximation.

Classical irreversible thermodynamics (CIT) assumes a linear dependence of the four-vector R^μ on the thermodynamics fluxes. In the Eckart frame it is possible to construct a generic four-vector R^μ from the thermodynamics fluxes and the four-velocity. This results in an entropy current for CIT given by,

$$\mathcal{S}^\mu = s\rho u^\mu + \frac{q^\mu}{T}. \tag{16}$$

The entropy generation rate from Eq. (14) must remain positive which, after some algebra, leads to the following relations for the thermodynamic fluxes under the assumption of an ideal EOS given by Eq. (4) (Takamoto & Inutsuka 2011),

$$q^\mu_{\rm NS} = \kappa \gamma^{\mu\nu}\left(\frac{\partial T}{\partial x_\nu} - \frac{T}{\rho h}\frac{\partial p}{\partial x_\nu}\right), \tag{17a}$$

$$\tau^{\mu\nu}_{\rm NS} = \pi^{\mu\nu}_{\rm NS} + \Pi_{\rm NS}\gamma^{\mu\nu},$$

$$\tau^{\mu\nu}_{\rm NS} = -\gamma^{\mu\rho}\gamma^{\nu\sigma}\left[\eta\left(\frac{\partial u_\rho}{\partial x_\sigma} + \frac{\partial u_\sigma}{\partial x_\rho} - \frac{2}{3}g_{\rho\sigma}\frac{\partial u^\lambda}{\partial x_\lambda}\right)\right] - \xi\frac{\partial u^\lambda}{\partial x_\lambda}\gamma^{\mu\nu}, \tag{17b}$$

that ensure the positivity of the entropy generation rate if the transport coefficients κ, η, and ξ are positive. These transport coefficients account for the thermal conductivity κ, the shear viscosity η, and the bulk viscosity ξ. The expressions in Eq. (17) are known as the constitutive equations of CIT. These equations will hereafter be referred to as the Navier–Stokes terms appearing in the non-perfect formulation, as indicated by the subscript NS.

Although these equations are written in covariant form, the theory of CIT exhibits undesirable tendencies which are attributed to the mathematical nature of this formulation. The constitutive equations from Eq. (17) posses a parabolic mathematical character which implies any disturbances in those fields can propagate at infinite speeds. Romatschke (2010) demonstrated this feature through a perturbation analysis, concluding that the diffusion speed was linearly proportional to the wave number which permits superluminal speeds and therefore violates a basic premise of relativity theory. High wave numbers were associated with instabilities in the numerical solution as found by Hiscock & Lindblom (1983). Therefore, the relativistic Navier–Stokes equations alone do not deliver a causal theory of physical dissipation in a relativistic fluid.

To overcome these troublesome numerical and physical deficiencies, the theory known as extended irreversible thermodynamics

(EIT) can be employed. After taking the divergence of the entropy four-current the second law of thermodynamics is again satisfied by imposing linear relations between the thermodynamic fluxes and extended forces. The most popular strategy for a more complete description of physical viscosity and heat conduction is found through the work of Israel & Stewart (1979). As a consequence of the Israel–Stewart phenomenological theory the dissipation variables for heat flow and viscosity are considered as independent variables that depend on convective derivatives of the dissipative variables themselves whilst ensuring that the entropy in the system does not decrease. This leads to a set of Israel–Stewart evolution equations which are presented in their truncated form according to Muronga (2007) as,

$$\hat{\mathcal{D}}\Pi = \frac{1}{\tau_\Pi}(\Pi_{\rm NS} - \Pi) - I_\Pi, \tag{18a}$$

$$\hat{\mathcal{D}}\pi^{\mu\nu} = \frac{1}{\tau_\pi}(\pi^{\mu\nu}_{\rm NS} - \pi^{\mu\nu}) - I^{\mu\nu}_\pi, \tag{18b}$$

$$\hat{\mathcal{D}}q^{\mu} = \frac{1}{\tau_q}(q^{\mu}_{\rm NS} - q^{\mu}) - I^{\mu}_q, \tag{18c}$$

where the convective derivative is defined as $\hat{\mathcal{D}} = u^\alpha \nabla_\alpha$. The source terms I_Π, $I^{\mu\nu}_\pi$, and I^μ_q represent the higher-order contributions to the entropy four-current $\mathcal{S}^\mu$ that are introduced through Israel–Stewart theory and τ_Π, τ_π, and τ_q are relaxation times. These correspond to the mean collision time, the inverse of which relates to the mean-free flight time of a particle. For astrophysical applications the source terms on the right-hand-side of Eq. (18) can be neglected such that simplified telegrapher equations emerge (Takamoto & Inutsuka 2011),

$$W\left(\frac{\partial}{\partial t} + v^j \frac{\partial}{\partial x^j}\right)\Pi = \frac{1}{\tau_\Pi}(\Pi_{\rm NS} - \Pi), \tag{19a}$$

$$W\left(\frac{\partial}{\partial t} + v^j \frac{\partial}{\partial x^j}\right)\pi^{\mu\nu} = \frac{1}{\tau_\pi}(\pi^{\mu\nu}_{\rm NS} - \pi^{\mu\nu}), \tag{19b}$$

$$W\left(\frac{\partial}{\partial t} + v^j \frac{\partial}{\partial x^j}\right)q^{\mu} = \frac{1}{\tau_q}(q^{\mu}_{\rm NS} - q^{\mu}), \tag{19c}$$

where the convective derivative has been written explicitly. Because the relaxation times depend on the collisions between constituent particles only cases close to equilibrium are considered since the continuum hypothesis is assumed. The relaxation times are computed using the dissipation transport coefficients Π, π, and κ and the coefficients β_0, β_1, and β_2 which should be computed from kinetic theory and are a unique property of a particular fluid. If the characteristic time-scale τ is much shorter than the fluid time-scale $\tau_{\rm fluid}$ then this results in a set of stiff equations. In this work the relaxation times are computed according to (Takamoto & Inutsuka 2011),

$$\tau_\Pi = \frac{72\xi}{\beta^2 p}, \quad \tau_\pi = \frac{3}{2}\frac{\eta}{p}, \quad \tau_q = \frac{5\kappa T}{4p} \quad \text{if} \quad \Gamma = \frac{4}{3}, \tag{20}$$

where $\beta = \rho/T$.

The numerical solution for non-perfect RHD is then found through Eqs. (13), (17), (19), and (20).

3 NUMERICAL METHODS

The numerical solver used in the present research is built upon a finite volume Godunov-type High-Resolution Shock-Capturing (HRSC) framework. This general methodology is extensively applied to RHD problems throughout the literature, recent developments are presented in an excellent review by Martí & Müller Martí & Müller (2015).

3.1 Numerical Flux Considerations

Computation of a numerical flux is required at the interface between each computation cell. In the present work we make use of an approximate Riemann, in particular, the HLL approximate Riemann solver of Harten et al. (1983). The HLL Riemann solver has proved itself as a standard workhorse in many RHD solvers due to the fact that it is exact for single shocks, easy to implement, and robust, i.e. not susceptible to the so-called Carbuncle problem when strong shocks are present (Quirk 1994). The HLL approximate Riemann solver assumes that only two waves emanate after the decay of an initial discontinuity; these waves represent either shock or rarefaction waves. As such, this Riemann solver does not resolve a contact discontinuity which is why this method is known to be more dissipative surrounding shear layers. To alleviate this issue the HLLC Riemann solver, originally devised by Toro et al. (1994), can be used to resolve the missing intermediate contact discontinuity. This methodology was subsequently extended to RHD and RMHD by Mignone & Bodo (2005) and Mignone & Bodo (2006), respectively. For the HLL Riemann solver used in the present work the reader may refer to Appendix A for its mathematical description.

3.2 Spatial Reconstruction

Initial conditions required for the solution of the aforementioned local Riemann problem are obtained by means of a spatial reconstruction method. The techniques used for this operation are as equally applicable to hyperbolic systems in classical hydrodynamics and relativistic hydrodynamics, hence modification of their original formulation is not required. If a piecewise constant representation is used, in other words, the initial conditions to the Riemann problem are obtained by the two neighboring cell averages, then any information contained within the cell is lost. To circumvent this information loss, a polynomial representation of the flow variables within each cell can be used that in turn provides better approximations for the left and right states required for the initial conditions of the local Riemann problem.

In the present work we evaluate the *Weighted Essentially Non-Oscillatory* (WENO) schemes, originally devised by Liu et al. (1994) from the extension of the ENO scheme proposed by Harten et al. (1987). WENO schemes are well-suited for problems containing discontinuities and complex smooth flow features. These schemes use a combination of adaptive stencils in which each stencil contains a polynomial constructed from the cell-averaged flow quantities, in the present work the reconstruction is performed using the primitive variables at each cell-center. The sub-stencils surround the interface for which the spatial reconstruction is being applied, i.e. where the Riemann problem is being solved. Then, the stencils are assigned a specific non-linear weight depending on the local smoothness surrounding each stencil. When a stencil contains non-smooth data, i.e. a discontinuity, its weight are set to, essentially, zero. On the other hand, when a solution contains smooth data, optimal weights are prescribed. This results in an weighted combination of the global stencil based on the polynomials constructed from each sub-stencil. The order of accuracy for WENO schemes is determined by the number of cells in each sub-stencil, k, such that the entire reconstruction polynomial is of order $(2k-1)$. For a detailed insight into the workings of WENO schemes the reader

is referred to Shu (1997), Shu (2003), Balsara & Shu (2000). For a summary of the WENO reconstruction schemes implemented for the present work the reader may refer to Appendix B.

Despite their early success and application to RHD, see e.g. Tchekhovskoy et al. (2007), Nunez-de la Rosa & Munz (2016), and Radice & Rezzolla (2012), it was noticed that for schemes with a theoretical order above five, the monotonicity properties of the schemes were lost. It was shown by Nunez-de la Rosa & Munz (2016) that one option is overcome this is to identify troubled regions surrounding discontinuities using a shock detector and then locally reduce the order of the WENO scheme. This approach is practical and requires minimal implementation effort whilst also providing robustness to the high-order schemes. Balsara & Shu (2000) were able to devise a new class of high-order WENO schemes with an additionally monotonocity preserving (MP) functionality (Suresh & Huynh 1997). This new breed of high-order WENO schemes were suitably named MP-WENO and demonstrated the desirable monotonocity preserving properties at orders higher than five. Although the MP procedure is applied to WENO orders above five by Balsara & Shu (2000), the MP procedure is applied to orders of five (inclusive) and above such that an MP-WENO5 and MP-WENO7 scheme is used in the present work, the third-order WENO3 scheme remains unchanged. The computational procedures for ensuring the reconstruction remains montontocity preserving are found in Appendix B4.

3.3 Temporal Evolution

To advance the hyperbolic system of conservation laws given by Eq. (9) forward in time, the method of lines is employed. The high-order methods discussed thus far only apply to the spatial discretization with no consideration for the time discretization strategy. This work relies on the explicit multi-stage Runge–Kutta method devised by Shu & Osher (1988). In particular, a third-order Runge–Kutta (RK3) method is used, which advances the solution from time-level t^n to time-level t^{n+1}. The third-order Runge–Kutta method remains TVD (Total Variation Diminishing) if the time-step is chosen according to,

$$\Delta t = \frac{\mathrm{CFL}}{Dim}\min\left(\frac{\Delta x^a}{|\lambda_a|}\right), \tag{21}$$

where Δx^a is the grid spacing and λ_a corresponds to the maximum wave speed from Eq. (10) in the directions: $a = \{1, 2, 3\} \equiv \{x, y, z\}$ and the variable Dim denotes the number of dimensions being modeled. Finally, the CFL (Courant–Friedrichs–Lewy) condition will maintain stability provided the constraint,

$$\mathrm{CFL} \leq 1, \tag{22}$$

is met. Only information from the current time-step is required for the TVD RK3 method so its implementation does not require large amounts of memory. The full TVD RK3 time integration method is summarized for completeness in Appendix C.

3.4 Implementation Strategy for Causal Non-Perfect RHD

To obtain a numerical solution that still permits the use of the Godunov-type HRSC methods used for perfect RHD, Eq. (13) is split into its comprising non-dissipative (perfect) and dissipative (viscous) part. The non-dissipative branch of the governing equations, Eq. (23), remains unchanged from Section 2.1. The dissipative arm of the governing equations then reads as,

$$\frac{\partial}{\partial t}\begin{pmatrix} D \\ S^i + q^0 u^i + q^i u^0 + \tau^{0i} \\ E - D + 2q^0 u^0 + \tau^{00} \end{pmatrix} + \frac{\partial}{\partial x^j}\begin{pmatrix} 0 \\ q^i u^j + q^j u^i + \tau^{ij} \\ q^0 u^j + q^j u^0 + \tau^{0j} \end{pmatrix} = 0. \tag{23}$$

The dissipative part in Eq. (23) contains the dissipative fluxes and components of the dissipation terms evolved in time as well as the usual conserved variables. The solution of the overall system is based on the strategy employed by Akamatsu et al. (2014) which was originally pioneered by Takamoto & Inutsuka (2011). A global set of conserved variables is defined as,

$$\boldsymbol{U} = \boldsymbol{U}_{\mathrm{perf}} + \boldsymbol{U}_{\mathrm{vis}}, \tag{24}$$

where,

$$\boldsymbol{U}_{\mathrm{perf}} = \begin{bmatrix} D \\ S^i \\ E - D \end{bmatrix}, \qquad \boldsymbol{U}_{\mathrm{vis}} = \begin{bmatrix} 0 \\ q^0 u^i + q^i u^0 + \tau^{0i} \\ 2q^0 u^0 + \tau^{00} \end{bmatrix}, \tag{25}$$

denote the conserved variables corresponding to the non-dissipative (perfect) and the dissipative (viscous) parts. Similarly, the primitive variables are also denoted as $\boldsymbol{V}_{\mathrm{perf}} = (\rho, u^i, p)^T$ and $\boldsymbol{V}_{\mathrm{vis}} = (q^\mu, \pi^{\mu\nu}, \Pi)^T$ for the non-dissipative and dissipative primitive variables, respectively.

Israel & Stewart (1979) devised that for a causal theory of dissipation, telegrapher equations for the dissipative variables were required. In the present work these are given by Eq. (19) which constitute a set of stiff equations meaning that the characteristic time-scale τ is much shorter than the fluid time-scale τ_{fluid}. If this is the case then stringent time-step restrictions must be imposed to guarantee the numerical solution remains stable. To ensure stability the time-step size must be shorter than the characteristic time-scale, i.e. $\Delta t \lesssim \tau \ll \tau_{\mathrm{fluid}}$. This is unfeasible for RHD in multiple dimensions as this would lead to unpractical computational costs. One possible solution is to use an implicit–explicit (IMEX) Runge–Kutta time integration method Pareschi & Russo (2005), see Mignone et al. (2019), Palenzuela et al. (2009), and Dionysopoulou et al. (2013) for applications of the IMEX scheme related to resistive RMHD. Stable numerical schemes for hyperbolic conservation laws have also been devised in Svärd & Mishra (2011) for the classical Euler equations with stiff source terms. In this work we use the approach presented by Takamoto & Inutsuka (2011) who proposed splitting Eq. (19) using the Strang-splitting method into an advection part and a relaxation (stiff) part. The advection equation reads,

$$\left(\frac{\partial}{\partial t} + v^j \frac{\partial}{\partial x^j}\right)\Pi = 0, \tag{26a}$$

$$\left(\frac{\partial}{\partial t} + v^j \frac{\partial}{\partial x^j}\right)\pi^{\mu\nu} = 0, \tag{26b}$$

$$\left(\frac{\partial}{\partial t} + v^j \frac{\partial}{\partial x^j}\right)q^\mu = 0, \tag{26c}$$

which is solved using a simple first-order upwind method. In the present work a high-resolution upwind method is used as recommended by Okamoto & Nonaka (2017). The remaining part of Eq. (19) is,

$$\frac{\partial}{\partial t}\pi^{\mu\nu} = \frac{\pi^{\mu\nu}_{\mathrm{NS}} - \pi^{\mu\nu}}{\tau_\pi W}, \tag{27a}$$

$$\frac{\partial}{\partial t}q^\mu = \frac{q^\mu_{\mathrm{NS}} - q^\mu}{\tau_q W}, \tag{27b}$$

$$\frac{\partial}{\partial t}\Pi = \frac{\Pi_{\mathrm{NS}} - \Pi}{\tau_\Pi W}, \tag{27c}$$

which constitutes the stiff equation. Following Takamoto & Inutsuka (2011), this can be solved in a stable manner using the Piecewise Exact Solution (PES) via,

$$\pi^{\mu\nu} = (\pi_0^{\mu\nu} - \pi_{\rm NS}^{\mu\nu}) \exp\left[-\frac{\Delta t}{\tau_\pi W} \right] + \pi_{\rm NS}^{\mu\nu}, \tag{28a}$$

$$q^{\mu} = (q_0^{\mu} - q_{\rm NS}^{\mu}) \exp\left[-\frac{\Delta t}{\tau_q W} \right] + q_{\rm NS}^{\mu}, \tag{28b}$$

$$\Pi = (\Pi_0 - \Pi_{\rm NS}) \exp\left[-\frac{\Delta t}{\tau_\Pi W} \right] + \Pi_{\rm NS}, \tag{28c}$$

where the subscript 0 denotes the value at the previous time-step. The terms denoted with the subscript NS refers to the Navier–Stokes dissipation variables which are found from Eq. (17). The time derivative in the calculation of the Navier–Stokes terms is achieved using a first-order explicit scheme and the spatial derivatives are found through use of central differencing.

The time-step for the case in which Israel–Stewart theory is invoked follows the provisional time-step proposed by Takamoto & Inutsuka (2011). They note that computing an exact time-step relation is difficult since the dissipative RHD equations are highly non-linear. The time-step used in this work which has demonstrated stable results thus far is given by,

$$\Delta t^{(1)} = \min\left(\frac{\Delta x_a}{|\lambda_a|} \right), \tag{29a}$$

$$\Delta t^{(2)} = \min\left(\Delta t^{(1)}, \frac{\Delta x_a^2}{\max(\eta, \xi, \kappa)} \right), \tag{29b}$$

$$\Delta t = \frac{\rm CFL}{Dim} \min\left(\Delta t^{(1)}, \Delta t^{(2)} \right). \tag{29c}$$

3.5 Primitive Variable Recovery

The conserved variables are the variables evolved in time by Eq. (2) and therefore a procedure is required to obtain the primitive variables. Unlike in classical hydrodynamics, a closed-form mapping between the conserved and primitive variables does not exist, hence an additional numerical effort is needed. The procedure of obtaining the primitive variable from the conserved ones is known as primitive variable recovery, whereby an additional procedure is implemented within the numerical code to do so. The primitive variable recovery algorithm is implemented within the developed high-order HRSC RHD code for an ideal EOS of the form $h = h(p, \rho)$ and follows that described by Mignone & Bodo (2005) which can be summarized as follows.

The relation between the primitive variables of interest $\boldsymbol{V} = (\rho, u^i, p)$ and the conserved variables is recalled as,

$$D = \rho W, \tag{30a}$$

$$S^i = \rho h W^2 u^i, \tag{30b}$$

$$E = \rho h W^2 - p - D, \tag{30c}$$

and the energy density in Eq. (30c) is also re-formulated such that $E = E + D$ before the primitive variable recovery procedure begins. An ideal gas is considered in the present work whereby the specific enthalpy takes the form,

$$h = 1 + \frac{p\Gamma}{\rho(\Gamma - 1)}. \tag{31}$$

The inverse relation of Eq. (30) resides in the solution of the non-linear equation for the pressure such that,

$$f(p) = p + E - \mathcal{X}\left[D + \frac{p\Gamma}{(\Gamma - 1)}\mathcal{X} \right] = 0, \tag{32}$$

where,

$$\mathcal{X} = \frac{1}{\sqrt{1 - |S^i|^2/(E + p)^2}}. \tag{33}$$

The function presented in Eq. (32) can be solved using a one-dimensional implicit Newton–Raphson root-finding procedure,

$$p^{n+1} = p^n - \frac{f(p^n)}{f'(p^n)}, \tag{34}$$

where the derivative of the function is,

$$f'(p) = 1 - \frac{\Gamma}{\Gamma - 1}\mathcal{X}^2 + \left[D + \frac{2\Gamma}{\Gamma - 1} p\mathcal{X} \right] \left[\frac{|S^i|^2}{(E + p)^3 \mathcal{X}^3} \right]. \tag{35}$$

Upon finding the pressure value within a acceptable region of accuracy, in this case when the difference in pressure from the previous Newton–Raphson iteration achieves the criterion $|p^{n+1} - p^n| < p^n \times 10^{-6}$, the remaining primitive variables are computed. The three-velocities are found through the relationship,

$$u^i = \frac{S^i}{(E + p)}, \tag{36}$$

from which the Lorentz factor is calculated accordingly. It then follows that the rest-mass density can be computed from,

$$\rho = \frac{D}{W}, \tag{37}$$

and finally the updated specific enthalpy is re-computed from Eq. (31) using the newly obtained primitive variables.

The above procedure applies only when the perfect RHD equations are considered. For the case of dissipative RHD in which the evolved conserved variables also include dissipative terms a minor modification in this procedure is required. Following the same logic used by Takamoto & Inutsuka (2011), the assumption that the computed four-velocity u^μ only experiences a very small change during the dissipative stage of the solution is made. Therefore, the dissipative conserved variables $\boldsymbol{U}_{\rm vis}$ are firstly computed by using the primitive variables after the inviscid step. Next, the perfect conserved variables are approximated by $\boldsymbol{U}_{\rm perf} = \boldsymbol{U} - \boldsymbol{U}_{\rm vis}$. The above procedure can then be applied, updating the calculated value of $\boldsymbol{U}_{\rm vis}$ using the newly obtain primitive variables at each iteration.

4 THE TWO-DIMENSIONAL RELATIVISTIC KELVIN–HELMHOLTZ INSTABILITY

4.1 Problem Setup

Initial conditions for the 2D relativistic Kelvin–Helmholtz instability closely follow those used by previous authors such as Beckwith & Stone (2011) and Radice & Rezzolla (2012) with the exception of the prescribed shear velocity, $V_{\rm shear}$. A periodic computational domain of size $[-0.5, 0.5] \times [-1, 1]$ is initialized with a uniform pressure field set to $p = 1$ with a low-density strip across the center of the domain. The shear velocity profile is then given by,

$$u^x(y) = \begin{cases} V_{\rm shear} \tanh[(y - 0.5)/a], & \text{if } y > 0, \\ -V_{\rm shear} \tanh[(y + 0.5)/a], & \text{if } y \leq 0, \end{cases} \tag{38}$$

in the x-direction with $a = 0.01$ as the characteristic size of the shear layer and $V_{\text{shear}} = 0.3$. A small perturbation in the transverse velocity component is prescribed using,

$$u^y(x,y) = \begin{cases} A_0 V_{\text{shear}} \sin(2\pi x) e^{\frac{-(y-0.5)^2}{\sigma}}, & \text{if } y > 0, \\ -A_0 V_{\text{shear}} \sin(2\pi x) e^{\frac{-(y+0.5)^2}{\sigma}}, & \text{if } y \leq 0, \end{cases} \tag{39}$$

where the perturbation amplitude is set to $A_0 = 0.1$ and $\sigma = 0.1$ is the characteristic length-scale. Note that the initial conditions for the rest-mass density field are uniform in the x-direction and are applied according to,

$$\rho(y) = \begin{cases} \rho_0 + \rho_1 \tanh[(y-0.5)/a], & \text{if } y > 0, \\ \rho_0 - \rho_1 \tanh[(y+0.5)/a], & \text{if } y \leq 0, \end{cases} \tag{40}$$

where $\rho_0 = 0.505$ and $\rho_1 = 0.495$.

The relativistic Kelvin–Helmholtz instability is used to study the contrasting behavior of the different high-order numerical schemes in conjunction with physically resolved shear viscosity. All numerical tests shown hereafter adopt a CFL number of 0.5 and the HLL approximate Riemann solver alongside the third-order TVD Runge–Kutta time integration method.

4.2 Flow Diagnostics

A systematic quantitative comparison between results is made using a selection of analysis techniques previously employed by various authors for similar investigations. In order to track the growth of the instability, the time evolution of the root-mean-square (RMS) value of the transverse velocity component is computed at regular time intervals throughout the simulation run. Following Radice & Rezzolla (2012), this is found from,

$$v_{\text{RMS}} = \langle |u^y|^2 \rangle \equiv \frac{1}{V} \int_V |u^y|^2 dV, \tag{41}$$

where V is the total volume of the computational domain. Dissipative properties of the numerical solution are monitored by consideration of two complementary strategies. The time evolution of the total kinetic energy in the system, found through the equation (Radice & Rezzolla 2012),

$$E_k(t) = \rho W(W-1), \tag{42}$$

is used to monitor any energy loss over time that may arise from numerical and/or physical dissipation. This technique was employed by San & Kara (2015) to study the dissipative properties of different numerical schemes in the context of the classical Euler equations. Any loss in kinetic energy found from the use of Eq. (42) will correspond to the total energy loss, i.e. numerical dissipation plus physical dissipation (if $\eta \neq 0$). If physical dissipation is not resolved then any dissipation comes as a result of numerical dissipation only. This result enables the direct analysis of the cumulative effect numerical and physical dissipation will have on the solution over time in a manner similar to what was achieved by Tsoutsanis et al. (2015) in the non-relativistic context.

Fig. 1 depicts an example of kinetic energy loss over time. The blue *reference* line corresponds to the maximum value of E_k at $t = 0$, hence if no dissipation whatsoever occurs during the numerical simulation then the kinetic energy would be constant over time. Note that Fig. 1 is qualitative in nature and only serves for illustration purposes. Eq. (42) is computed using the initial conditions. Therefore, the reference solution represents an idealized, fictive, case. The *red* and *yellow* lines provide an example of what

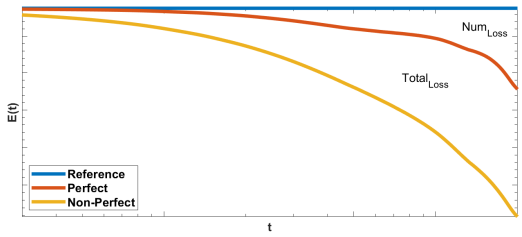

Figure 1. Example of the time evolution of kinetic energy computed from Eq. (42). The area between the blue and red line (Num$_{\text{Loss}}$) corresponds to energy lost due to numerical dissipation. The area between the blue yellow line (Total$_{\text{Loss}}$) corresponds to the total energy lost due to numerical and physical dissipation. Note that Fig. 1 is qualitative in nature and only serves for illustration purposes.

the decay of kinetic energy could potentially be over time when a perfect ($\eta = 0$) and non-perfect ($\eta \neq 0$) fluid are used, respectively. This analysis is only used at early simulation times until $t = 2$, at which time the instability is still experiencing its linear growth phase. To quantify the volume-averaged amount of kinetic energy lost during this time due to numerical dissipation the expression,

$$\text{Num}_{\text{Loss}} = \frac{1}{V}\left(E_{\text{Reference}} - E_{\text{Perfect}}\right) \tag{43}$$

is used which corresponds to the region in Fig. 1 between the blue and red line—this is only applicable when a perfect fluid ($\eta = 0$) is used. When a non-perfect fluid is used, the loss in kinetic energy is due to both physical and numerical dissipation, which is defined as Total$_{\text{Loss}}$ and given by,

$$\text{E}_{\text{Loss}} = E_{\text{Reference}} - E_{\text{Non-Perfect}}. \tag{44}$$

The kinetic energy lost due to physical dissipation alone, Viscous$_{\text{Loss}}$, i.e. the region between the red and yellow line from Fig. 1, is approximated from,

$$\text{Viscous}_{\text{Loss}} \approx \text{E}_{\text{Loss}} - \text{Num}_{\text{Loss}}. \tag{45}$$

Eq. (45) can only be considered an approximation because the numerical methods used for the evaluation of the non-perfect equations will also add numerical viscosity to the solution.

To quantify the small-scale structures appearing in the developed flow profile, the rest-mass density power spectrum is computed at selected flow times in the same manner as by Radice & Rezzolla (2012). This method was originally proposed by Beckwith & Stone (2011) to estimate the inherent numerical viscosity of a code. Smaller-scale structures can be smeared out by dissipative schemes so by quantifying to what extent they appear in the solution provides insight into the ability of a scheme to resolve complex, intricate flow structures. The 1D integrated power spectra for a given quantity, in this case the rest-mass density $\rho(x,y)$, is defined as,

$$P_\rho(k) = \int_{-1}^{1} |\hat{\rho}(k,y)|^2 dy, \tag{46}$$

where k is the wave number and,

$$\hat{\rho}(k,y) = \int_{-1/2}^{1/2} \rho(x,y) e^{-2\pi i k x} dx, \tag{47}$$

is the 1D Fourier transform of ρ which is computed using the Fast Fourier Transform (FFT) algorithm in Matlab. Finally, following the aforementioned previous authors, the rest-mass density power

spectrum is normalized according to,

$$\sum_{k=1}^{NX/2} P_\rho(k) = 1, \tag{48}$$

where NX is the number of grid points in the x-direction.

To complement the quantitative analysis, contour plots of the rest-mass density field are also shown where appropriate to provide qualitative insight into the behavior of the numerical solution.

5 THE INVISCID RELATIVISTIC KELVIN–HELMHOLTZ INSTABILITY

The invsicid case is considered first whereby $\eta = 0$. An initial grid resolution study was performed in which the RMS value of the velocity y-component from Eq. (41) was used to determine the growth of the instability. The inset of Fig. 2 reports the v_{RMS} using the WENO3 scheme and HLL Riemann solver for different grid resolutions. It is evident that the coarser grid resolutions produce a smaller instability growth whereas the two finest resolutions provide similar v_{RMS} profiles for the linear growth stage, i.e. until time $t \approx 2.5$. From this simple analysis it is concluded that the grid resolution of 512×1024 provides adequate spatial (grid) resolution which can be used as a base grid for subsequent analysis. The main result in Fig. 2 conveys the v_{RMS} at the grid resolution 512×1024 using the numerical schemes described so far. Considering again the linear growth stage, the higher-order MP-WENO schemes show the best agreement with one another whilst also reporting the steepest growth whereas the WENO3 and MUSCL2 (which we include as a low-order comparative) schemes report successively shallow growth profiles.

The rest-mass density contours at time $t = 4$, i.e. when the linear growth stage has finished, are found in Fig. 3. Perhaps the most striking difference between the reported snapshots is the occurrence of secondary flow features for the higher-order MP-WENO5 and MP-WENO7 schemes in Figs. 3c and 3d, respectively. Radice & Rezzolla (2012) attributed these secondary flow features to the numerical schemes themselves yet they were reported only for full-wave Riemann solvers; here the HLL Riemann solver is used which does not resolve the intermediate contact discontinuity in the Riemann fan. The lower-order MUSCL2 and WENO3 schemes in Figs. 3a and 3b, respectively, lack the appearance of any secondary flow feature. Subtle differences are present in the amount of vortex rotation present yet their qualitative features appear starkly different from the disorganized and intricate flow structure that develops for the higher-order schemes.

In an attempt to quantity the flow structures of the instability in the inviscid case from Fig. 3, the power spectra for the rest-mass density profiles is computed according to Eqs. (46), (47), and (48). The rest-mass density power spectra for all considered numerical schemes is found in Fig. 4. A clear difference in the computed profiles can be seen which indicates the higher-order schemes posses a lower numerical dissipation characteristic than their lower-order counterparts. This dissipation is however purely numerical and arises due to the numerical scheme and grid resolution. The MP-WENO7 scheme emerges as the least dissipative whereas the MUSCL2 scheme appears as the most dissipative. Fig. 4 then supports the rest-mass density contours in Fig. 3 which demonstrate how the higher-order schemes are capable of resolving smaller, complex flow features in the inviscid case where $\eta = 0$. Whether the secondary flow features can be deemed physical or not remains to be concluded and requires the inclusion of physical viscosity

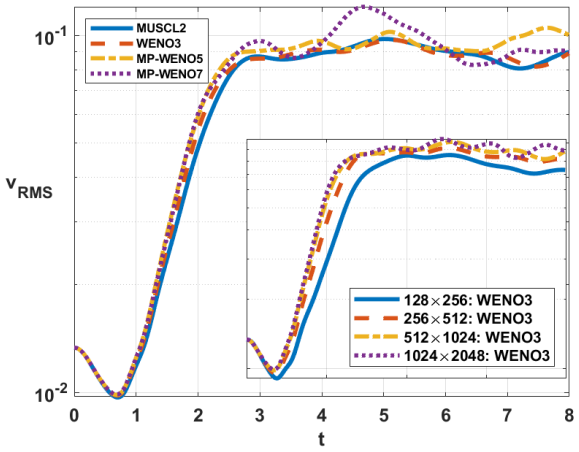

Figure 2. Evolution of the v_{RMS} for all numerical schemes when $\eta = 0$ using a grid resolution of 512×1024. The inset shows the effect of grid refinement when the WENO3 spatial reconstruction method is used. The HLL Riemann solver is used throughout.

for this to be realized and understood (Radice & Rezzolla 2012). Furthermore, this finding also offers a glimpse into what role the numerical viscosity plays regarding the initial growth of the instability. From Fig. 2 it was seen that the high-order schemes reported a steeper increase in the v_{RMS} value, similarly the inset showed how a finer grid resolution predicted a steeper growth of the v_{RMS}. It then possible to conclude that the high-order schemes predict an increased growth-rate compared to the lower-order schemes using the same grid which can be attributed to the amount of numerical dissipation present.

6 ON ESTIMATING NUMERICAL VISCOSITY USING PHYSICAL VISCOSITY

In a recent study, Obergaulinger & Aloy (2020) postulated that due to the resemblance in nature of physical and numerical viscosity, scaling relations to estimate the effective numerical viscosity of a code could be determined by establishing relationships from results achieved both with and without the inclusion of physical viscosity. A relationship was found by tracking the growth of the non-relativistic Kelvin–Helmholtz instability over (early) time. Differences between a solution at a very fine resolution and those at a coarser resolution or with physical viscosity present revealed a pattern that indicated numerical and physical viscosity both had a similar effect on the solution in terms of the instability growth. From this they were able to conclude a scaling correlation between physical and numerical viscosity. With this in mind, an investigation is conducted to evaluate this general hypothesis: numerical viscosity is capable of effectively mimicking physical viscosity. Following this, an attempt is made to measure the numerical viscosity present in the solution using physically resolved viscosity using the same reasoning given by Obergaulinger & Aloy (2020).

The time evolution of the kinetic energy according to Eq. (42) is used as the measurement parameter in this investigation, as opposed to Obergaulinger & Aloy (2020) who made use of the instability growth. If numerical viscosity can mimic physical viscosity then one could argue that there should exist a correlation between the amount of energy dissipated through either mechanism—this is basic premise of the current investigation. Three simulations are

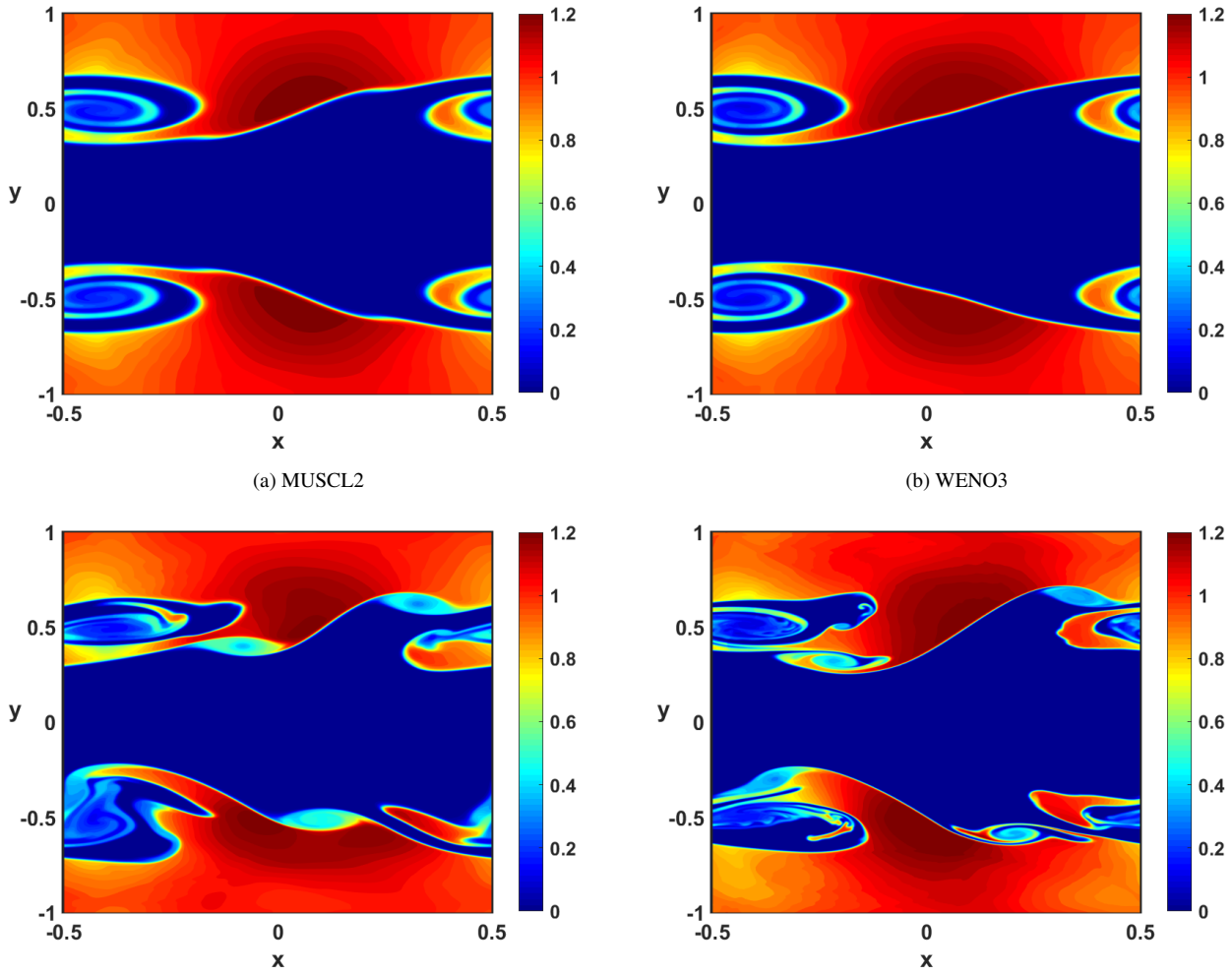

(a) MUSCL2

(b) WENO3

(c) MP-WENO5

(d) MP-WENO7

Figure 3. Rest-mass density contours at $t = 4$ for the MUSCL2 (3a), WENO3 (3b), MP-WENO5 (3c) and MP-WENO7 (3d) numerical schemes when physical viscosity was not resolved, i.e. $\eta = 0$. For all cases the HLL approximate Riemann solver was used with a grid resolution of 512×1024.

performed when $\eta = 0$, i.e. only numerical dissipation is present, using grid resolutions of 512×1024, 256×512, and 128×256. A further three simulations are performed when $\eta \neq 0$ using a finer grid resolution of 1024×2048, i.e. both numerical dissipation (although to a lesser extent) and physical dissipation are present. This method is applied to simulations using the WENO3, MP-WENO5, and MP-WENO7 spatial reconstruction schemes. A trial and error procedure then ensues to fathom an agreeable value of η using the fine resolution run to match the decay of kinetic energy in the simulations where $\eta = 0$ at the three coarser grid resolutions. In other words, a physical viscosity is prescribed such that the resulting decay of kinetic energy matches that of a solution where physical viscosity is not present but achieved using a coarser resolution. Fig. 5 depicts the attempts to match the decay of kinetic energy using the fine resolution and non-zero η with the results obtained at coarser resolutions and $\eta = 0$. A perfect matching is not always attainable, especially when a match is sought for the coarsest grid resolution. Note that the results have been scaled through consideration of the grid resolution, therefore these results only serve to match the trend of the kinetic energies and not the specific values.

6.1 Numerical Viscosity Estimations for WENO Reconstruction

Using the raw data corresponding to the data presented in Fig. 5, the volume-average total kinetic energy loss is calculated for each case using Eq. (44), this quantity is hereafter referred to as $\mathrm{E_{Loss}}$. This step enables the kinetic energies to be directly compared and since the loss rates are considered to be approximately equal then so should the volume average of total kinetic energy loss. These findings are listed in Tables 1, 2, and 3 for the WENO3, MP-WENO5, and MP-WENO7 schemes, respectively.

A power-law relation is found of the form $y = ax^b$ by considering $x \equiv \mathrm{NX}$ as the free variable, and when $x \equiv \eta$. Therefore, a scaling relation providing an approximate value of kinetic energy loss using either NX or η as an input is found. The scaling relation is found using a simple power-law of the form

$$\mathrm{E_{Loss}} \approx ax^b \tag{49}$$

where either $x \equiv \eta$ or $x \equiv \mathrm{NX}$ and have coefficients denoted with subscripts 1 and 2 (see Tables 4 and 5), respectively. Equating the left-hand-side of Eq. (49) with subscript 1 to the same expression

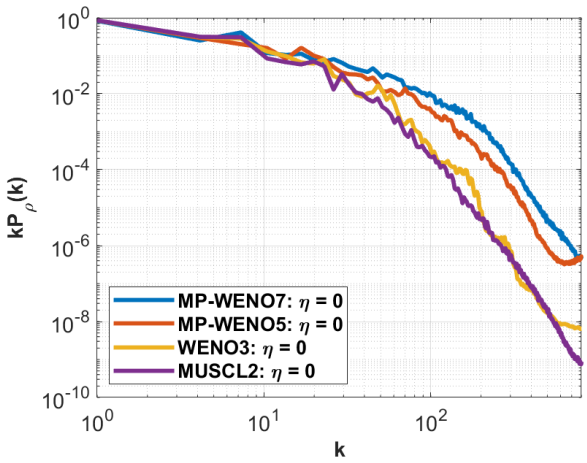

Figure 4. The rest-mass density power spectrum at $t = 4$ when $\eta = 0$ for all numerical schemes considered using a grid resolution of 512×1024.

Δx	η	E_{Loss}
1/1024	6×10^{-5}	1.18×10^{4}
1/1024	3×10^{-4}	3.47×10^{4}
1/1024	1.5×10^{-3}	7.88×10^{4}
1/512	0	1.26×10^{4}
1/256	0	3.62×10^{4}
1/128	0	8.58×10^{4}

Table 1. Volume-averaged total energy losses for the cases using the WENO3 scheme.

Δx	η	E_{Loss}
1/1024	3.0×10^{-5}	8.71×10^{5}
1/1024	1.5×10^{-5}	2.18×10^{4}
1/1024	7.5×10^{-5}	6.55×10^{4}
1/512	0	8.17×10^{5}
1/256	0	1.99×10^{4}
1/128	0	5.88×10^{4}

Table 2. Volume-averaged total energy losses for the cases using the MP-WENO5 scheme.

with subscript 2 gives rise to a formula relating η and NX such that

$$\eta \approx \left(\frac{a_2}{a_1}\mathrm{NX}^{b_2}\right)^{\frac{1}{b_1}}, \tag{50}$$

where the coefficients are problem, grid, and scheme-dependent. Fig. 6 depicts this relationship and how it could be used to predict the inherent numerical viscosity of the schemes for this problem. As expected, the plot shows that a finer grid resolution results in a smaller numerical viscosity and vice versa. The same figure also includes the relationship found when the MP-WENO5 and MP-WENO7 schemes are studied. The coefficients for Eq. (50) for the WENO3, MP-WENO5, and MP-WENO7 schemes are found in Tables 4 and 5.

Δx	η	E_{Loss}
1/1024	5.0×10^{-6}	4.35×10^{5}
1/1024	2.5×10^{-5}	7.05×10^{5}
1/1024	1.25×10^{-4}	1.88×10^{4}
1/512	0	4.27×10^{5}
1/256	0	5.73×10^{5}
1/128	0	2.78×10^{4}

Table 3. Volume-averaged total energy losses for the cases using the MP-WENO7 scheme.

WENO3		MP-WENO5		MP-WENO7	
a_1	b_1	a_1	b_1	a_1	b_1
0.047	0.615	0.083	0.68	0.013	0.461

Table 4. Coefficients for $x \equiv \eta$ using Eq. (49).

WENO3		MP-WENO5		MP-WENO7	
a_2	b_2	a_2	b_2	a_2	b_2
0.482	−1.313	0.796	−1.475	0.206	−1.4

Table 5. Coefficients for $x \equiv \mathrm{NX}$ using Eq. (49).

6.2 Flow Analysis

Given the estimated value of numerical viscosity found from the technique presented in Sec. 6.1, we consider what influence this may have on the flow dynamics. Rest-mass density contours at $t = 2$ are shown using the corresponding values of η and grid resolution for the WENO3, MP-WENO5, and MP-WENO7 schemes in Figs. 7, 8, and 9, respectively.

In the case of the WENO3 scheme in Fig. 7, differences between the numerical solution are apparent only upon close inspection.

Looking at the rest-mass density power spectrum in Fig. 10b, a complementary picture can be built that highlights an important difference between numerical and physical viscosity. The first two pairs considered in Figs. 7a and 7d, and Figs. 7b and 7e do not contain any obvious differences immediately discernible by eye. The final pair in Figs. 7c and 7f, on the other hand, present a more obvious difference. This is reflected in the rest-mass density power spectrum where the latter pair demonstrates less agreement, particularly at the larger scales. This indicates that although the overall dissipation of kinetic energy is deemed to be approximately the same for solutions at a fine grid resolution and a prescribed physical viscosity compared with those with no physical viscosity at coarser resolutions, a correlation between the actual flow structure is not always achievable. This highlights the different roles numerical and viscosity play on the evolution of the instability and serves as evidence that the contributions from numerical viscosity due to the grid resolution and numerical scheme do not have the same overall effect on the solution. Furthermore, it also indicates a lower bound for the applicability of predicting the numerical viscosity through Eq. (50) with any degree of confidence and that the formula is best applied to the two higher resolutions considered.

In addition, Fig. 11 reports the v_{RMS} evolution for the aforementioned η and grid resolution cases when the WENO3 and MP-WENO5 scheme is employed. At early time until $t = 2$ the relevant

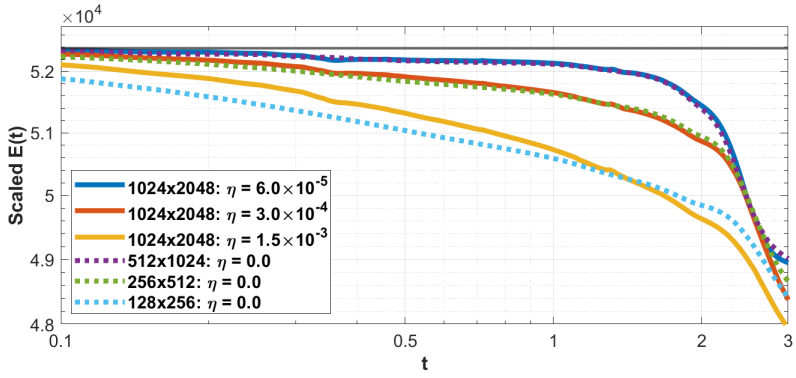

(a) WENO3

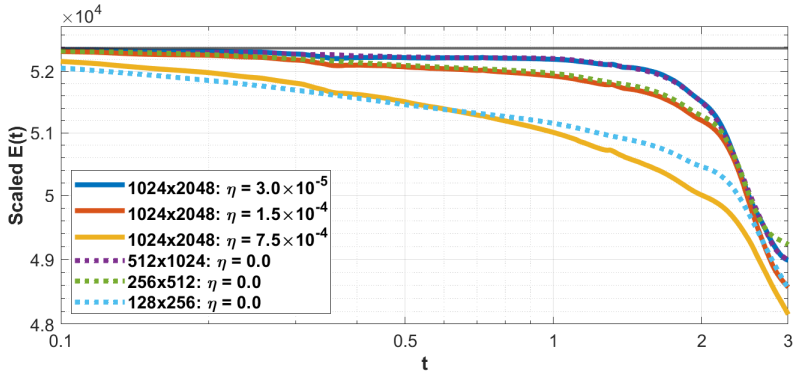

(b) MP-WENO5

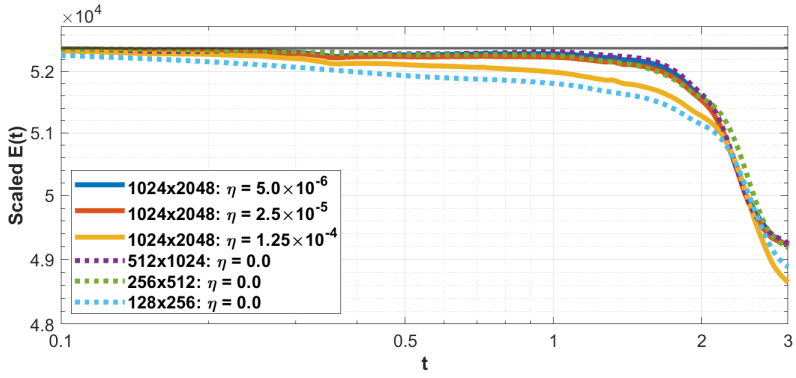

(c) MP-WENO7

Figure 5. Time-evolution of the total kinetic energy in the system at different grid resolutions and different values of η for the WENO3 (5a), MP-WENO5 (5b), and MP-WENO7 (5c) schemes.

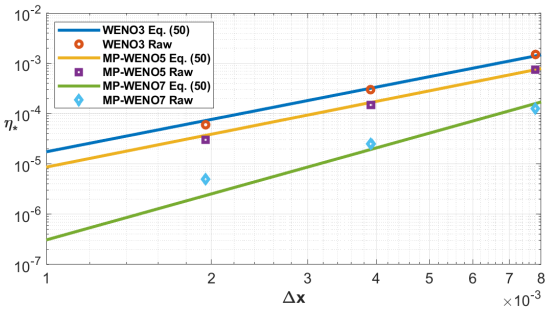

Figure 6. The predicted numerical viscosity as a function of grid spacing computed from Eq. (50) for the WENO3, MP-WENO5, and MP-WENO7 schemes.

pairs demonstrate good agreement, an indication that the technique applied in Obergaulinger & Aloy (2020) applies here also.

Considering the rest-mass density contours for the MP-WENO5 and MP-WENO7 schemes in Figs. 8 and 9, it is clear that secondary flow structures appear throughout the solutions, sometimes even when physical viscosity is resolved. Fig. 10b provides the rest-mass density power spectrum for the MP-WENO5 case. Disparity between the spectra is even more apparent when compared to what was found for the WENO3 case. As indicated by previous authors, in particular by Radice & Rezzolla (2012), these secondary flow features are not expected to appear from the initial conditions adopted in this article but arise as a consequence of the numerical schemes themselves. In these cases we are employing the HLL approximate Riemann solver for the numerical flux computations, hence we are not using a Riemann solver capable of resolving the

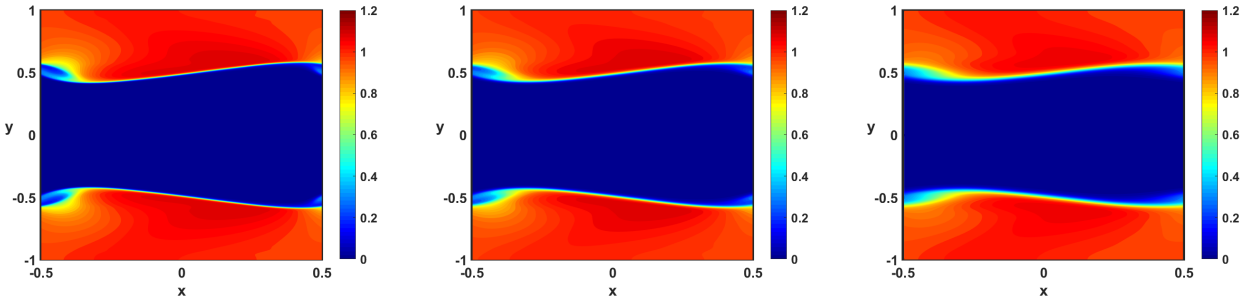

(a) 512×1024: $\eta = 0$ (b) 256×512: $\eta = 0$ (c) 128×256: $\eta = 0$

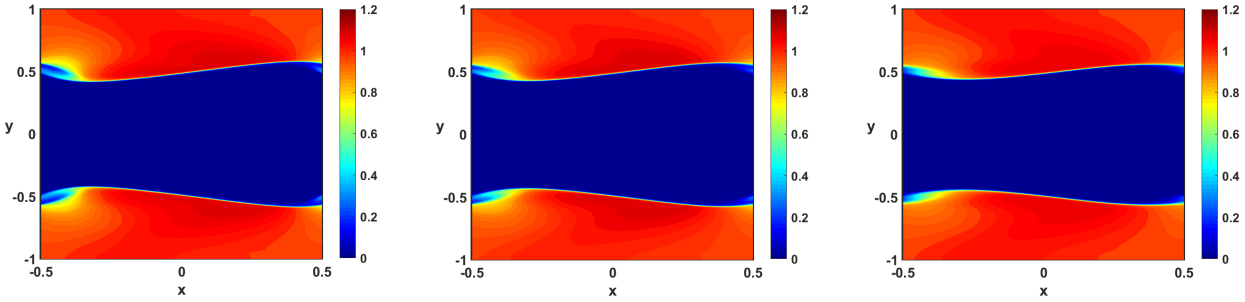

(d) 1024×2048: $\eta = 6 \times 10^{-5}$ (e) 1024×2048: $\eta = 3 \times 10^{-4}$ (f) 1024×2048: $\eta = 1.5 \times 10^{-3}$

Figure 7. Rest-mass density contours at $t = 2$ for the WENO3 scheme at different resolutions and values of η.

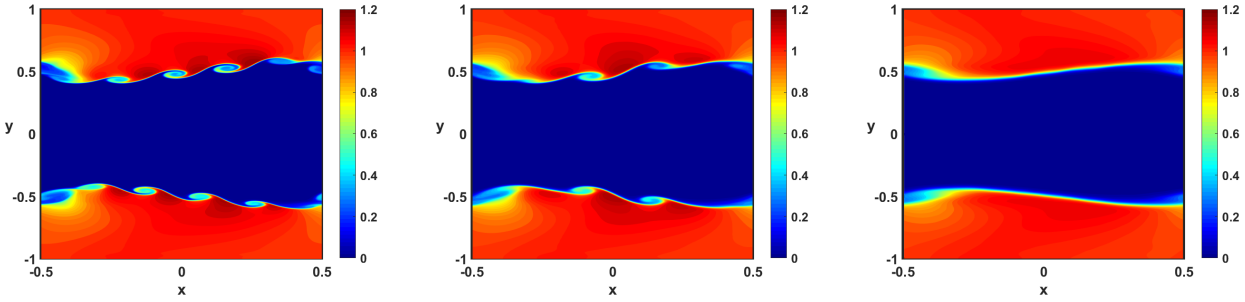

(a) 512×1024: $\eta = 0$ (b) 256×512: $\eta = 0$ (c) 128×256: $\eta = 0$

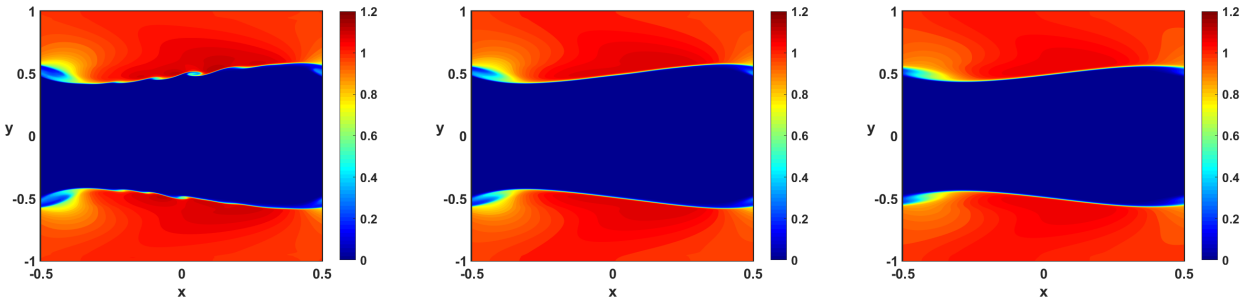

(d) 1024×2048: $\eta = 3 \times 10^{-5}$ (e) 1024×2048: $\eta = 1.5 \times 10^{-4}$ (f) 1024×2048: $\eta = 7.5 \times 10^{-4}$

Figure 8. Rest-mass density contours at $t = 2$ for the MP-WENO5 schemes at different resolutions and values of η.

intermediate contact discontinuity within the Riemann fan, which was suggested as the culprit for this behavior by Radice & Rezzolla (2012). Therefore, the secondary flow features shown here must arise due to the spatial reconstruction schemes. What remains to be seen is whether these secondary structures are genuine flow features captured by the numerical scheme or if they are purely a numerical artifact.

Given a physical viscosity or an estimated value of the numerical viscosity, we choose the center of momentum frame to calculate a numerical Reynolds number. Using the unperturbed state, the velocity of the frame is found to be $u_{\rm F} = 0.0355c$, which corresponds

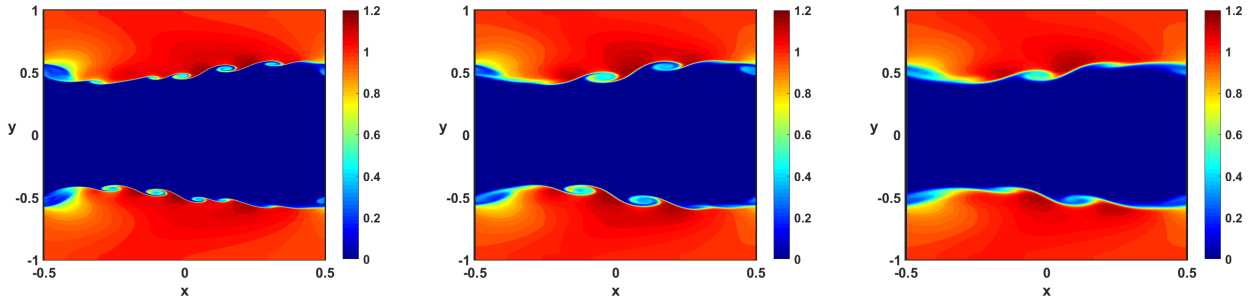

(a) 512 × 1024: $\eta = 0$ (b) 256 × 512: $\eta = 0$ (c) 128 × 256: $\eta = 0$

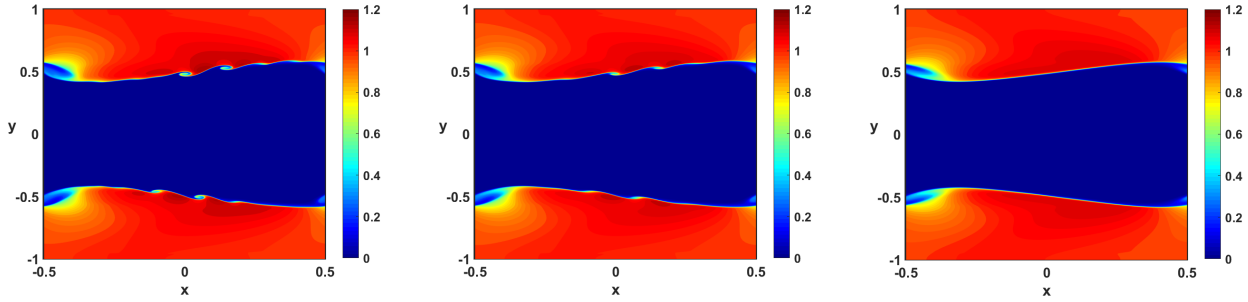

(d) 1024 × 2048: $\eta = 5 \times 10^{-6}$ (e) 1024 × 2048: $\eta = 2.5 \times 10^{-5}$ (f) 1024 × 2048: $\eta = 1.25 \times 10^{-4}$

Figure 9. Rest-mass density contours at $t = 2$ for the MP-WENO7 schemes at different resolutions and values of η.

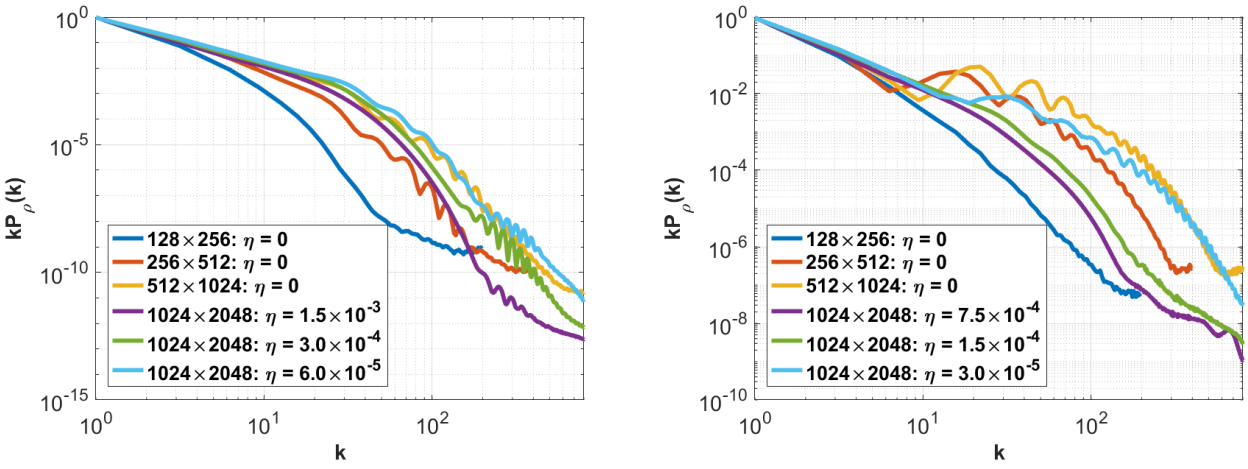

(a) WENO3 (b) MP-WENO5

Figure 10. Rest-mass density power spectra for different grid resolutions and values of η for the WENO3 (10a) and MP-WENO5 (10b) schemes.

to a frame Lorentz factor transforming to the center of momentum frame of $W_{\rm F} = 1.0006$. A numerical grid-scale Reynolds number can then be determined through,

$$Re_* = \frac{\rho u' W_{\rm F}^2 \Delta x}{\eta_*}, \tag{51}$$

where η_* denotes the numerical viscosity, which could also be replaced with physical viscosity if available, and u' represents velocity fluctuations found through the calculation of the velocity difference in adjacent computational cells. A more traditional definition of the Reynolds number for a relativistic fluid was given by Richardson & Chung (2002), however they did not specify what considerations should be given to the chosen frame of reference.

Contours of the local grid-scale numerical Reynolds number can be seen in Figs. 12a–12c based on findings for the MP-WENO7 scheme, where secondary flow features are found to occur, and the WENO3 scheme, in which secondary flow features are absent. Considering the contour gradation in the shear region, we find that the numerical cell Reynolds number approaches unity surrounding the shear layer when secondary flow features are absent. This is further illustrated in Figs. 12d–12f which show a center-line profile of the Reynolds number through the domain. Indeed, we see that for the cases where secondary flow features are absent, the Reynolds number is less than, or approaches unity. When using the MP-WENO7 scheme however, the Reynolds number is much greater than unity in this region. Since in a numerical calculation we cannot

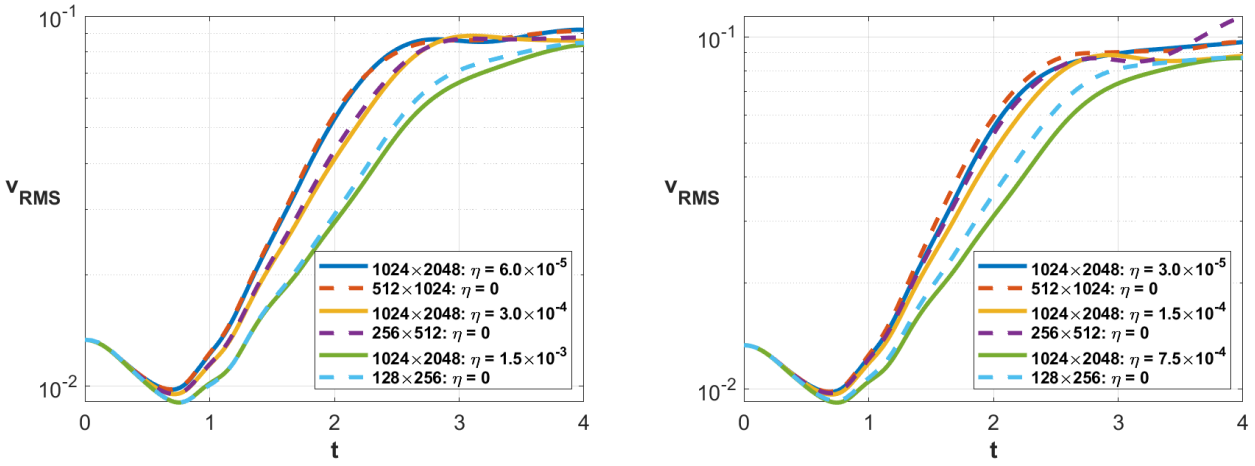

(a) WENO3 (b) MP-WENO5

Figure 11. Evolution of the v_{RMS} for different grid resolutions and values of η for the WENO3 (11a) and MP-WENO5 (11b) schemes.

describe the spatial scale comparable to Δx it is therefore logical that the grid-scale numerical Reynolds number approaches unity or lower for any grid-scale perturbations to be avoided.

To further understand whether these secondary flow features are physical or not, an additional grid refinement study is reported in Fig. 13 for each WENO scheme with a given value of η. The value of η is chosen according the estimations at the preceding level of grid resolution. In all cases, an absence of secondary flow structures is found for the finer grid resolutions. A similar finding is made by Radice & Rezzolla (2012) who also note that these features tend to disappear as the resolution is increased. This indicates that the secondary features are non-physical since as the grid resolution increases we should also witness a more accurate numerical solution, as well as a lower amount of inherent numerical viscosity.

For the results in which we do not observe any secondary flow instabilities we find that the local numerical Reynolds number at the cell size is on the order of unity surrounding the shear layer, $\rho u W^2 \Delta x/\eta_* \sim 1$. This means that physical viscosity is comparable to the numerical viscosity at any scale described in the simulation, hence grid-scale perturbations that result in secondary flow features are absent. In this numerical experiment, we arrive at the important conclusion that to obtain a physically correct solution we should include physical viscosity and increase the resolution so that we keep the physical Reynolds number at the cell size surrounding shear flow features on the order of unity or lower. Although secondary flow features may appear when a Riemann solver capable of resolving the intermediate contact discontinuity is used, such as the HLLC or HLLD, it is likely that the dissipation properties of these schemes is the sole culprit for the non-physical behavior since we find that such features appear when spatial reconstruction schemes with low numerical dissipation are employed.

7 AN ACCURACY AND COST EVALUATION OF HIGH-ORDER SCHEMES WITH PHYSICAL VISCOSITY

One such motivation behind the usage of high-order methods resides in the computational requirements necessary to resolve accurate flow physics, i.e. computational time and memory considerations. In other words, it is advantageous to apply numerical methods with the smallest truncation error and largest discretization to reduce the computational burden otherwise imposed from extremely fine grid resolutions (Rezzolla & Zanotti 2013).

To evaluate this claim, we consider solutions obtained using a fine grid resolution and low-order spatial reconstruction method compared with those using a coarser resolution and a high-order spatial reconstruction method. It has been shown already that secondary flow structures can appear in the solution for the inviscid case depending on the numerical scheme used, see also Mignone et al. (2009), Beckwith & Stone (2011), Radice & Rezzolla (2012). This feature means that the growth of the instability may not converge in the non-dissipative case (Takamoto & Inutsuka 2011). Therefore, to provide a more consistent evaluation two considerations are made. Firstly, the HLL approximate Riemann solver is used throughout which is known to be more dissipative than its full-wave counterparts, but is less susceptible to the development of numerical grid-scale perturbations. Secondly, to further ensure that such numerical perturbations remain absent in the numerical solution, the schemes/grid resolutions are compared with a fixed η throughout. This means that achieving a converged solution across the different numerical schemes is more likely when these factors are considered. Although the solutions obtained at a coarse resolution will not always be able to capture the flow structures on the smallest scale due to the constraints imposed by the grid, the larger structures which are still dependent on the prescribed shear viscosity and inherent numerical viscosity are hoped to be replicated.

Fig. 14 shows the rest-mass density contours of the relativistic Kelvin–Helmholtz instability at $t = 4$ using the HLL approximate Riemann solver and a shear viscosity parameter of $\eta = 1 \times 10^{-3}$. This is a choice of η is known through experimentation to be large enough to suppress any secondary flow features yet small enough not to completely dampen the overall instability growth. Seemingly, the results demonstrate good qualitative agreement when the high-order, coarse resolution solutions (Figs. 14a, 14c) are compared with the low-order, fine resolution solutions (Figs. 14b, 14d). Fig. 15 shows the time evolution of v_{RMS} for which good agreement can be seen between the growth of the instability between the solutions obtained. The instability growth at an even coarser resolution of 256×512 at high-order is comparable with the findings of solutions using resolution 512×1024 using lower-order schemes for which little difference can be seen between results. Similarly, the inset

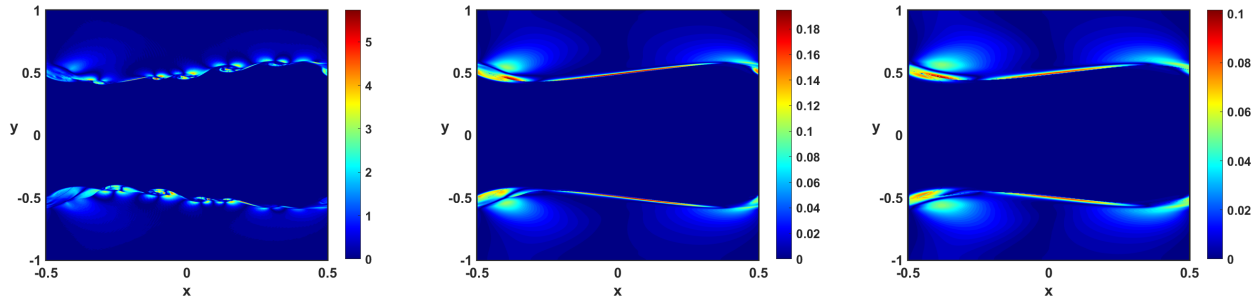

(a) Local Reynolds number: MP-WENO7, 512×1024, $\eta_* = 5 \times 10^{-6}$

(b) Local Reynolds number: WENO3, 512×1024, $\eta_* = 6 \times 10^{-5}$

(c) Local Reynolds number: WENO3, 256×512, $\eta_* = 3 \times 10^{-4}$

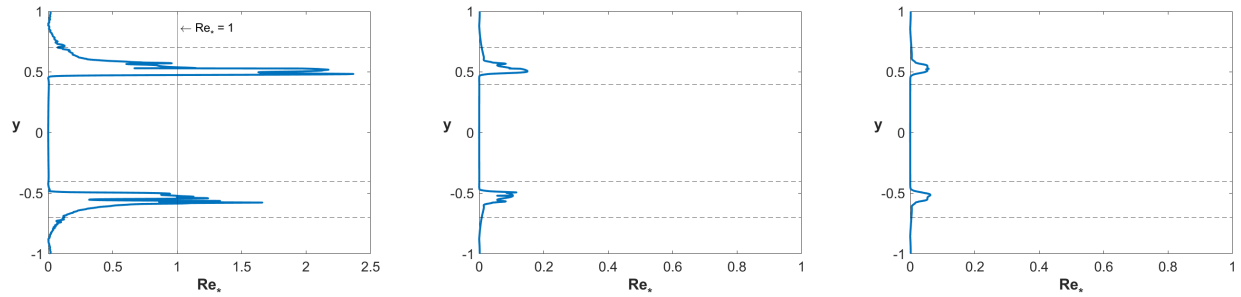

(d) Center-line local Reynolds number profile: MP-WENO7, 512×1024, $\eta_* = 5 \times 10^{-6}$

(e) Center-line local Reynolds number profile: WENO3, 512×1024, $\eta_* = 6 \times 10^{-5}$

(f) Center-line local Reynolds number profile: WENO3, 256×512, $\eta_* = 3 \times 10^{-4}$

Figure 12. Numerical local grid-scale numerical Reynolds number contours at $t = 2$ and center-line profiles.

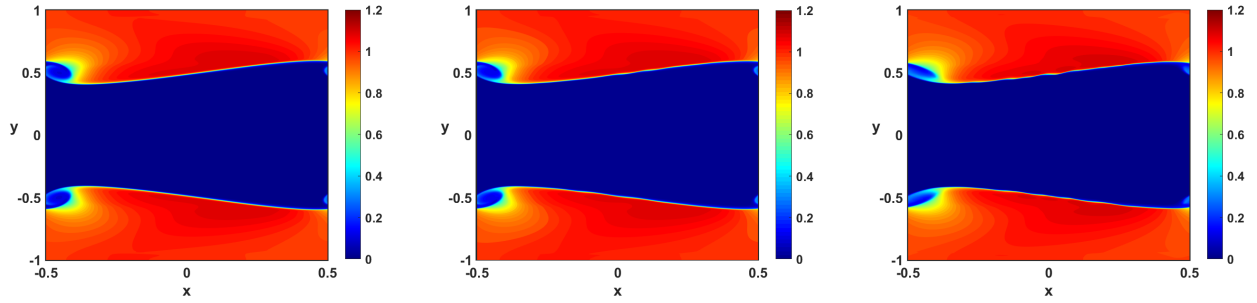

(a) WENO3: $\eta = 6 \times 10^{-5}$

(b) MP-WENO5: $\eta = 3 \times 10^{-5}$

(c) MP-WENO7: $\eta = 5 \times 10^{-6}$

Figure 13. Rest-mass density contours at $t = 2$ for the WENO schemes at a finer grid resolution of 2048×4096 and finite values of η.

shows this evolution of those cases presented in Fig. 14, demonstrating that negligible difference is found between results in terms of the instability growth.

To further extend this analysis the power spectrum of the rest-mass density for the instability at $t = 4$ is shown in Figs. 16a and 16b. Naturally, the results obtained with the finer resolution are able to capture smaller-scale features when compared with the coarser resolutions. Therefore, it is only possible here to make general overall comparisons between schemes at inertial, intermediate, wave numbers. The results obtained for the range of numerical schemes differ marginally in their rest-mass density power spectrum however they do report consistent power spectra across the different grid resolutions. Interestingly, the MP-WENO7 scheme at the lower grid resolutions reports the least dissipation in this range. These findings offer a positive insight into the performance of high-order schemes at coarser resolutions in terms of their quantitative accuracy when contrasted with lower-order schemes at finer grid resolutions. To further support this finding, the additional volume-average kinetic energy losses due to the inclusion of physical viscosity are shown in Fig. 17, which is computed from Eq. (45) until $t = 2$. It is apparent that the amount of volume-averaged kinetic energy loss considered demonstrates a degree convergence for all schemes at finer grid resolutions. What is interesting is the rate of convergence of each individual numerical scheme. It can be seen that the higher-order schemes converge to the ultimate value of kinetic energy loss at a faster rate with respect to the grid resolution, meaning that the physical viscosity contribution is solved more accurately at coarser resolution when a high-order scheme is used. This supports the conjecture that due to the more accurate solutions achieved during the perfect fluid step when a high-order scheme is used which subsequently feeds into the dissipative part, a more accurate overall solution can be attained.

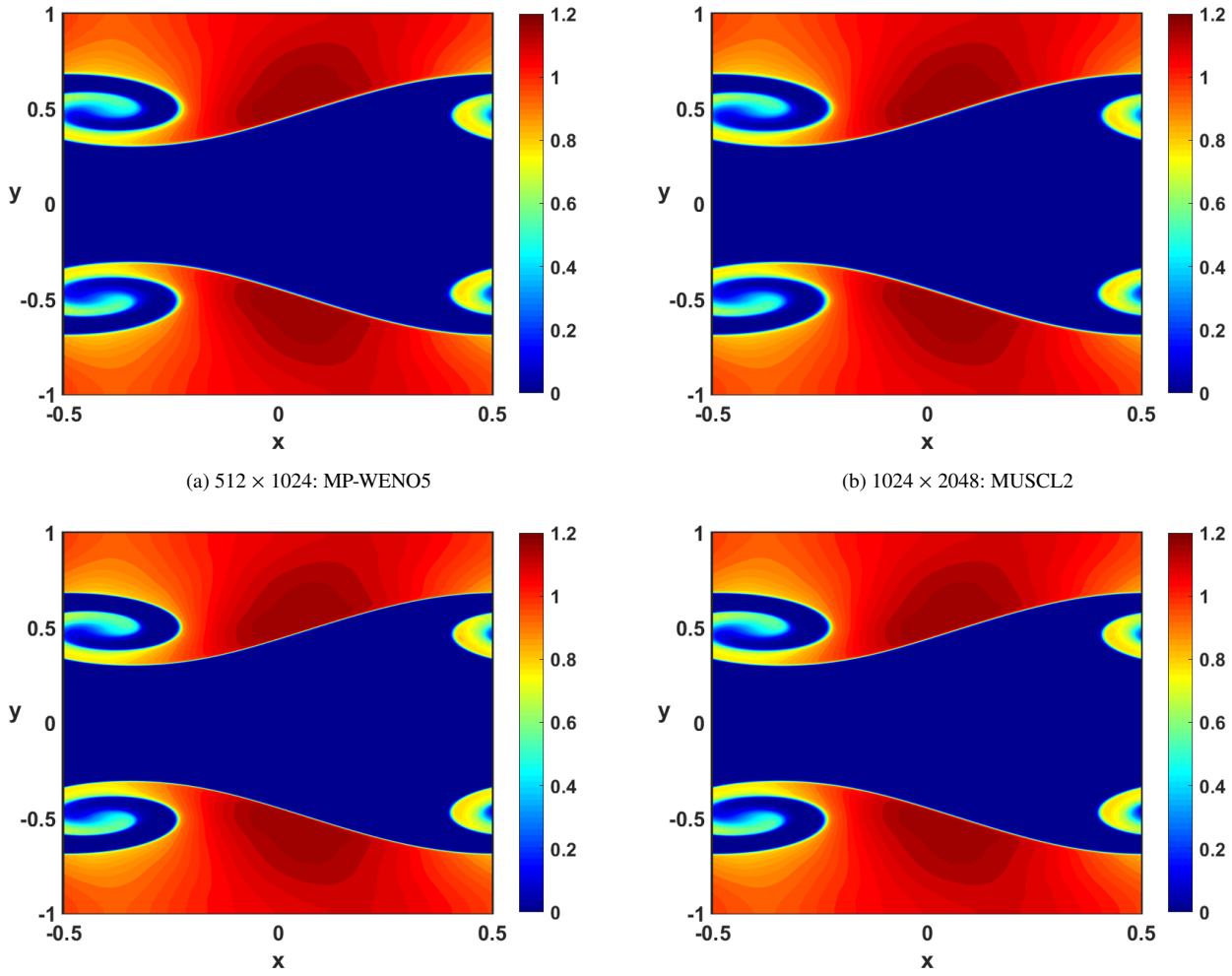

(a) 512 × 1024: MP-WENO5

(b) 1024 × 2048: MUSCL2

(c) 512 × 1024: MP-WENO7

(d) 1024 × 2048: WENO3

Figure 14. Rest-mass density contours of the relativistic Kelvin–Helmholtz instability at $t = 4$. The solutions are obtained using the HLL approximate Riemann solver and a shear viscosity parameter of $\eta = 10^{-3}$. The solutions using a coarse grid resolution of 512 × 1024 and a higher-order scheme (left) are seen in Figs. 14a and 14c whilst the results obtained with a finer grid resolution and lower-order scheme (right) are seen in Figs. 14b and 14d.

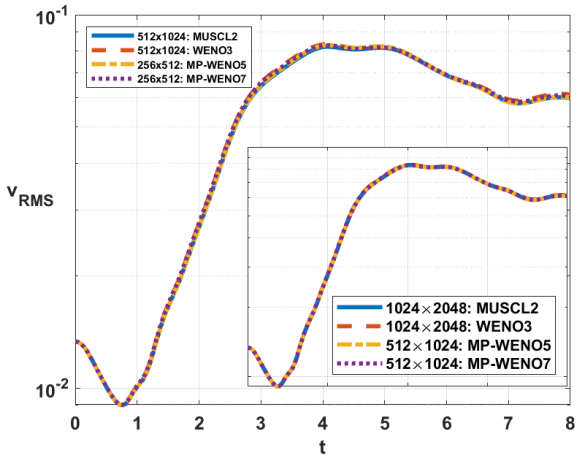

Figure 15. Evolution of the v_{RMS} and the volume-averaged kinetic energy loss contribution arising from the inclusion of viscosity for different numerical schemes at different grid resolutions using $\eta = 10^{-3}$.

Finally, the computational timings for the numerical schemes and grid resolutions used are considered. Table 6 provides the normalized CPU timings with respect to the computational time required by the MUSCL2 scheme at the finer resolution. The WENO3 scheme is found to be approximately 20% less computationally expensive than the MUSCL2 scheme at the finest grid resolution however for the base/practical grid their difference is only marginal. Most notably is the computational saving found when the higher-order scheme is used on a coarser grid. When the MP-WENO5 scheme is used on the coarser grid, the computational burden is only about 17% of that required by the MUSCL2 scheme at the finer resolution. Furthermore, the MP-WENO7 requires about 18% of that time. The computational savings found by deploying the higher-order scheme on a coarser mesh are relatively substantial and could therefore contribute to the decision of which numerical scheme and grid size are most-suitable for certain numerical investigations.

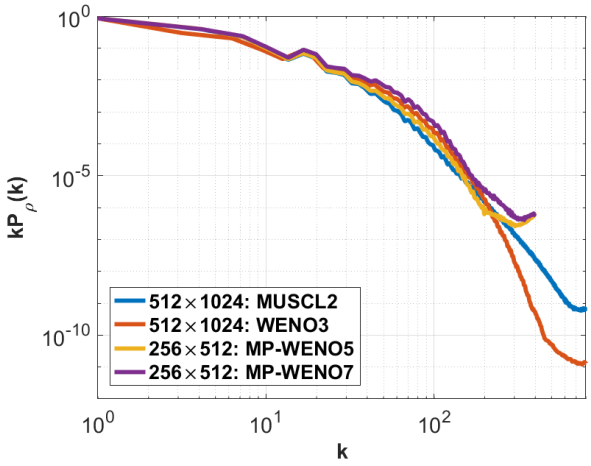

(a) Coarser grid comparative.

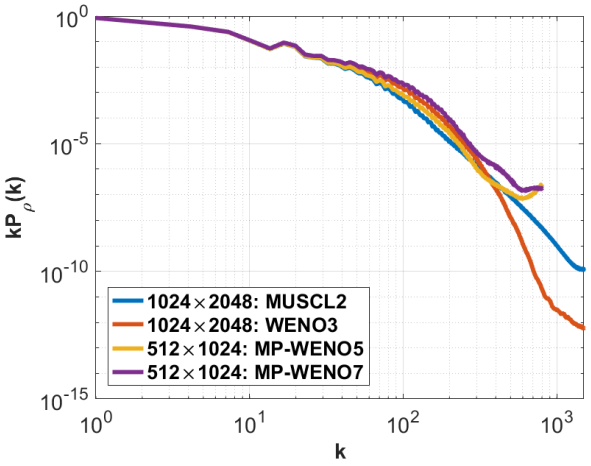

(b) Finer grid comparative.

Figure 16. The rest-mass density power spectrum at $t = 4$ using high-order schemes at coarse grid resolutions and low-order schemes at fine grid resolutions.

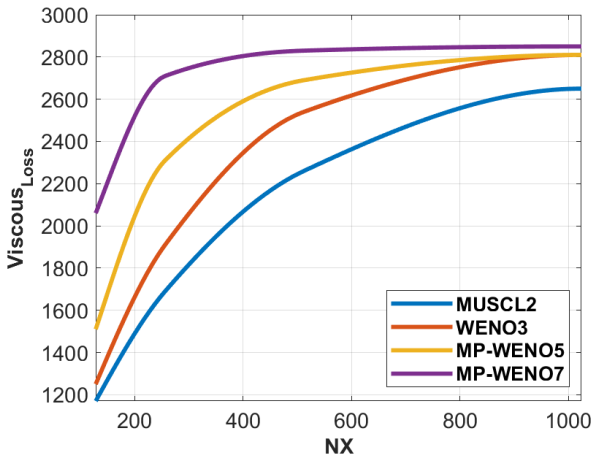

Figure 17. Energy Losses due to viscous dissipation.

Grid Size	Scheme	Normalized CPU Time
1024 × 2048	MUSCL2	1
1024 × 2048	WENO3	0.798
512 × 1024	MP-WENO5	0.168
512 × 1024	MP-WENO7	0.187
512 × 1024	MUSCL2	1
512 × 1024	WENO3	0.984
256 × 512	MP-WENO5	0.169
256 × 512	MP-WENO7	0.178

Table 6. Normalized CPU time with respect to the MUSCL2 scheme for the high vs low-order schemes presented in this section.

8 CONCLUSIONS

Numerical solutions to the non-perfect (dissipative) RHD equations using a causal theory of physical dissipation have been presented using a finite volume high-resolution shock-capturing (HRSC) Godunov-type framework. The kinetic energy decay is employed as a flow diagnostic to provide an estimation of the numerical dissipation of high-order schemes based on results obtained both with and without physically resolved dissipation for three orders of WENO reconstruction. Based on the premise that numerical viscosity can effectively mimic physical viscosity, an empirical relationship between the grid spacing Δx and the numerical shear viscosity η_* for the WENO3, MP-WENO5, and MP-WENO7 scheme were established. This technique is problem and scheme-dependent and requires a trial and error procedure to fathom the correct relationships between the dissipation of kinetic energy arising from numerical and physical dissipation. To perform the same analysis using a different strategy for evaluating the numerical flux, such as the HLLC approximate Riemann solver, which is known to be produce less numerical dissipation than the HLL approximate Riemann solver, is recommended as a future work. It is also noted that although dissipation arising from the kinetic energy loss could be matched, one should be cautious about assuming numerical and physical viscosity have the same overall effect on the solution. It was found that despite this correlation, differences between other flow properties such as the instability growth-rate and formation did differ.

It has been found that for the higher-order numerical schemes, namely the MP-WENO5 and MP-WENO7, the secondary flow features were present even when physical shear viscosity was resolved. To understand whether these flow features were physical attributes of the flow physics or purely numerical artifacts, two further tests were performed. Firstly, the same simulations with physical viscosity, albeit a small amount, were re-performed using a very fine grid resolution. A reduction in the size of the secondary flow features was then visible, indicating that the secondary flow features were likely caused by grid-scale perturbations. From this experiment, we found that the secondary features vanished, giving credence to the theory that such features are numerical artifacts and that physically resolved viscosity is required to achieve a converged solution. Secondly. it has also been found that in order to ensure a converged solution of the relativistic Kelvin–Helmholtz instability, one should seed the numerical solution with enough physical shear viscosity such that the physical cell Reynolds number at the shear layer approaches unity. This was found through a new definition of the numerical relativistic Reynolds number in the center of momentum frame.

High-order methods may offer the prospect to save computational time, because it is possible to use a higher-order scheme at a coarser spatial resolution and still achieve global flow-field properties as when a low-order scheme at a finer resolution is used. This hypothesis was tested using the relativistic Kelvin–Helmholtz instability when a value of physical viscosity was prescribed such that a converged solution could be achieved, i.e. the physical viscosity would be enough to damp any artificial grid-scale perturbations. It has been found that the high-order methods used herein offered this performance advantage if the macroscopic properties of the flow are what an investigator is placing emphasis on and resulted in an approximate computational saving of 80%. Additional test problems such as those involving shock-waves are recommended to be further investigated as a future work.

ACKNOWLEDGEMENTS

This work was partially conducted as a JSPS International Research Fellow (Graduate School of Science, Nagoya University) [JSPS Summer Program 2019, SP19122]. Further financial support was provided by JSPS KAKENHI grant Nos. 16H02160, 18H05436, 18H05437 and the Centre for Computational Engineering Sciences at Cranfield University under the project code EEB6001R.

DATA AVAILABILITY STATEMENT

All data incorporated into the present article is available upon request. The data underlying this article will be shared upon reasonable request to the corresponding author.

REFERENCES

Abbott B. P., et al., 2017a, Physical Review Letters, 119, 30
Abbott B. P., et al., 2017b, The Astrophysical Journal, 848, L13
Abdikamalov E., Zhaksylykov A., Radice D., Berdibek S., 2016, Monthly Notices of the Royal Astronomical Society, 461, 3864
Akamatsu Y., ichiro Inutsuka S., Nonaka C., Takamoto M., 2014, Journal of Computational Physics, 256, 34
Baier R., Romatschke P., 2007, European Physical Journal C, 51, 677
Baiotti L., Rezzolla L., 2017, Reports on Progress in Physics, 80
Baiotti L., Giacomazzo B., Rezzolla L., 2009, Classical and Quantum Gravity, 26
Balsara D. S., Shu C. W., 2000, Journal of Computational Physics, 160, 405
Banyuls F., Font J. A., Ibanez J. M., Marti J. M., Miralles J. A., 1997, The Astrophysical Journal, 476, 221
Beckwith K., Stone J. M., 2011, The Astrophysical Journal Supplement Series, 193, 6
Bodo G., Mignone A., Rosner R., 2004, Physical Review E - Statistical Physics, Plasmas, Fluids, and Related Interdisciplinary Topics, 70, 4
Boris J. P., Book D. L., 1973, Journal of Computational Physics, 11, 38
Bucciantini N., Del Zanna L., 2006, Astronomy and Astrophysics, 454, 393
Chabanov M., Rezzolla L., Rischke D. H., 2021, Monthly Notices of the Royal Astronomical Society, stab1384
Chandra M., Gammie C. F., Foucart F., Quataert E., 2015, The Astrophysical Journal, 810, 162
Cowperthwaite P. S., et al., 2017, The Astrophysical Journal, 848, L17
Del Zanna L., et al., 2013, European Physical Journal C, 73, 1
Dionysopoulou K., Alic D., Palenzuela C., Rezzolla L., Giacomazzo B., 2013, Physical Review D - Particles, Fields, Gravitation and Cosmology, 88, 1
Drout M. R., et al., 2017, Science, 358, 1570
Eckart C., 1940, Physical Review, 58, 919
Ferrari A., Trussoni E., Zaninetti L., 1978, Astronomy and Astrophysics, 64, 43
Harten A., Lax P. D., van Leer B., 1983, SIAM Review, 25, 35
Harten A., Engquist B., Osher S., Chakravarthy S., 1987, Journal of Computational Physics, 71, 231
Hiscock W., Lindblom L., 1983, Annals of Physics, 151
Israel W., Stewart J. M., 1979, Annals of Physics, 118, 341
Karpenko I., Huovinen P., Bleicher M., 2014, Computer Physics Communications, 185, 3016
Kiuchi K., Kyutoku K., Sekiguchi Y., Shibata M., 2018, Physical Review D, 97, 124039
Landau L., Lifshitz E., 1987, Fluid Mechanics, doi:10.1016/B978-0-08-033933-7.50001-5.
Liu X.-D., Osher S., Chan T., 1994, Journal of Computational Physics, 115, 200
Martí J. M., Müller E., 2015, Living Reviews in Computational Astrophysics, 1, 182
Martí J. M., Müller E., Font J. A., Ibáñez J. M., Marquina A., 1997, The Astrophysical Journal, 479, 151
Mignone A., Bodo G., 2005, Monthly Notices of the Royal Astronomical Society, 364, 126
Mignone A., Bodo G., 2006, Monthly Notices of the Royal Astronomical Society, 368, 1040
Mignone A., Ugliano M., Bodo G., 2009, Monthly Notices of the Royal Astronomical Society, 393, 1141
Mignone A., Mattia G., Bodo G., Del Zanna L., 2019, Monthly Notices of the Royal Astronomical Society, 486, 4252
Mourão Roque V. R., Lugones G., 2018, Journal of Cosmology and Astroparticle Physics, JCAP03
Muronga A., 2007, Physical Review C - Nuclear Physics, 76, 1
Nunez-de la Rosa J., Munz C. D., 2016, Monthly Notices of the Royal Astronomical Society, 460, 535
Obergaulinger M., Aloy M.-Á., 2020, Numerical viscosity in simulations of the two-dimensional Kelvin-Helmholtz instability (arXiv:2001.01927), arxiv:2001.01927
Okamoto K., Nonaka C., 2017, European Physical Journal C, 77, 1
Okamoto K., Akamatsu Y., Nonaka C., 2016, European Physical Journal C, 76
Palenzuela C., Lehner L., Reula O., Rezzolla L., 2009, Monthly Notices of the Royal Astronomical Society, 394, 1727
Pareschi L., Russo G., 2005, Journal of Scientific Computing, 25
Quirk J. J., 1994, International Journal for Numerical Methods in Fluids, 18, 555
Radice D., Rezzolla L., 2012, Astronomy & Astrophysics, 547
Radice D., Rezzolla L., 2013, The Astrophysical Journal, 766, L10
Rana Z. A., Thornber B., Drikakis D., 2011, Physics of Fluids, 23
Rembiasz T., Obergaulinger M., Cerdá-Durán P., Aloy M.-Á., Müller E., 2017, The Astrophysical Journal Supplement Series, 230, 32
Rezzolla L., Zanotti O., 2013, Relativistic Hydrodynamics, first edn. Oxford University Press
Ricci F., Silva P. A., Tsoutsanis P., Antoniadis A. F., 2020, Aerospace Science and Technology, 97, 105648
Richardson G. A., Chung T. J., 2002, The Astrophysical Journal Supplement Series, 139, 539
Romatschke P., 2010, International Journal of Modern Physics E, 19, 1
Roy V., Chaudhuri A. K., 2012, Physical Review C - Nuclear Physics, 85, 1
San O., Kara K., 2015, Computers and Fluids, 117, 24
Schenke B., Jeon S., Gale C., 2010, Physical Review C - Nuclear Physics, 82, 1
Schenke B., Jeon S., Gale C., 2011, Physical Review Letters, 106, 1
Shu C.-w., 1997, Technical Report 97-65, Essentially Non-Oscillatory and Weighted Essentially Non-Oscillatory Schemes for Hyperbolic Conservation Laws Operated by Universities Space Research Association. (arXiv:1001246X), doi:10.1007/BFb0096355
Shu C. W., 2003, International Journal of Computational Fluid Dynamics, 17, 107
Shu C.-W., Osher S., 1988, Journal of Computational Physics, 77, 439

Siegel D. M., Ciolfi R., Harte A. I., Rezzolla L., 2013, Physical Review D - Particles, Fields, Gravitation and Cosmology, 87, 1
Suresh A., Huynh H. T., 1997, Journal of Computational Physics, 136, 83
Svärd M., Mishra S., 2011, Journal of Computational and Applied Mathematics, 235, 1564
Takamoto M., Inutsuka S.-i., 2011, Journal of Computational Physics, 230, 7002
Tchekhovskoy A., McKinney J. C., Narayan R., 2007, Monthly Notices of the Royal Astronomical Society, 379, 469
Tian C., Chen Y., 2016, The Astrophysical Journal, 824
Toro E. F., Spruce M., Speares W., 1994, Shock Waves, 4, 25
Townsend J. F., Könözsy L., Jenkins K. W., 2020, Monthly Notices of the Royal Astronomical Society, 496, 2493
Tsoutsanis P., Kokkinakis I. W., Könözsy L., Drikakis D., Williams R. J. R., Youngs D. L., 2015, Computer Methods in Applied Mechanics and Engineering, 293, 207
Zhang W., MacFadyen A., Wang P., 2009, The Astrophysical Journal, 692, L40
Zrake J., MacFadyen A., 2013, The Astrophysical Journal Letters, 763

APPENDIX A: HLL APPROXIMATE RIEMANN SOLVER

The numerical fluxes required for the solution of Eq. (2) are obtained via the solution of a local Riemann problem at a cell boundary. The flux through the cell boundary at $x_{i-\frac{1}{2}}$, where x_i is the cell-center, is written as $\mathbf{F}_{\mathbf{i-\frac{1}{2}}}$ and found from initial data

$$\mathbf{U}(\mathbf{x},\mathbf{0}) = \begin{cases} \mathbf{U}_{\mathbf{L},\mathbf{i-\frac{1}{2}}} & \text{if } x < x_{i-\frac{1}{2}} \\ \mathbf{U}_{\mathbf{R},\mathbf{i-\frac{1}{2}}} & \text{if } x > x_{i-\frac{1}{2}} \end{cases} \tag{A1}$$

where $\mathbf{U}_{\mathbf{L},\mathbf{i-\frac{1}{2}}}$ and $\mathbf{U}_{\mathbf{R},\mathbf{i-\frac{1}{2}}}$ are the values to the left and to the right of the cell boundary, respectively. The numerical flux across that boundary is computed by means of an exact or approximate Riemann solver.

The HLLE Riemann solver, hereafter HLL, assumes that after the initial discontinuity decay, only two waves emanate that propagate in opposite directions with velocities S_L and S_R leaving a constant single-state in-between. With knowledge of the smallest and largest characteristic wave speeds, i.e. $S_L \leq 0$ and $S_R \geq 0$, the numerical flux at the cell boundary can be computed via

$$\mathbf{F}_{\mathbf{i}\pm\frac{1}{2}} = \begin{cases} \mathbf{F_L} & \text{if } \ 0 \leq S_L, \\ \mathbf{F}^{\mathrm{HLL}} & \text{if } \ S_L \leq 0 \leq S_R, \\ \mathbf{F_R} & \text{if } \ 0 \geq S_R, \end{cases} \tag{A2}$$

where $\mathbf{F_L} = \mathbf{F}(\mathbf{U_L})$, $\mathbf{F_R} = \mathbf{F}(\mathbf{U_R})$ and $\mathbf{F}^{\mathrm{HLL}}$ is the numerical HLL flux in the constant intermediate state given by

$$\mathbf{F}^{\mathrm{HLL}} = \frac{\mathbf{S_R F_L} - \mathbf{S_L F_R} + \mathbf{S_L S_R}(\mathbf{U_R} - \mathbf{U_L})}{\mathbf{S_R} - \mathbf{S_L}}. \tag{A3}$$

S_L and S_R should be chosen via

$$S_L := \min\big(0, S_-(\mathbf{U_L}), \mathbf{S}_-(\mathbf{U_R})\big), \tag{A4a}$$

$$S_R := \max\big(0, S_+(\mathbf{U_L}), \mathbf{S}_+(\mathbf{U_R})\big), \tag{A4b}$$

where S_- and S_+ are provided by the expressions in Eq. (10).

APPENDIX B: WENO RECONSTRUCTION SCHEMES

The fundamental components of the WENO reconstruction schemes used in the present work are summarized. For a more detailed discussion and explanation the reader is referred to Shu (2003). In what follows we only provide the necessary expressions for a practical implementation.

A reconstruction is required at the point

$$u_{i-\frac{1}{2}} = \sum_{k=1}^{N+1} \omega_k u^{(k)}_{i-\frac{1}{2}} \tag{B1}$$

where $\omega_k \geq 0$ and $\sum_{k=1}^{N+1} \omega_k = 1$. The non-linear weight ω_k is defined by,

$$\omega_k = \frac{\tilde{\omega}_k}{\sum_{i=1}^{N} \tilde{\omega}_i}, \tag{B2}$$

where,

$$\tilde{\omega}_k = \frac{\gamma_k}{(\epsilon + \beta_k)^2}. \tag{B3}$$

The parameter ϵ is used to avoid division by zero and is typically chosen to be $\epsilon = 10^{-6}$. The smoothness indicators are represented by β_k and γ_k denotes the so-called linear weights. The superscript N refers to the degree of the individual WENO polynomials The smoothness indicators and linear weights are provided for each choice of WENO reconstruction used in the present work. The reconstructed variables in the present work are the primitive variables, from which we use the cell averages on a grid of uniform spacing,

$$\bar{u}_i = \frac{1}{\Delta x} \int_{x_{i-\frac{1}{2}}}^{x_{i+\frac{1}{2}}} u(x) dx. \tag{B4}$$

The reconstructions are provided for the right initial condition of the local Riemann problem at $x_{i-\frac{1}{2}}$, which is denoted by $u^{\mathrm{R}}_{i-\frac{1}{2}}$, and similarly the left initial condition at $x_{i+\frac{1}{2}}$, which is denoted by $u^{\mathrm{L}}_{i+\frac{1}{2}}$. To obtain the initial conditions at the locations $u^{\mathrm{L}}_{i-\frac{1}{2}}$ and $u^{\mathrm{R}}_{i+\frac{1}{2}}$, one need only shift the given expressions for $u^{\mathrm{L}}_{i+\frac{1}{2}}$ and $u^{\mathrm{R}}_{i-\frac{1}{2}}$ one place to the left and right, respectively. For the implementation in the present work, the reconstruction is performed on the primitive variables ρ, u^i, and p.

B1 WENO3

The reconstructed right state $u^{\mathrm{R}}_{i-\frac{1}{2}}$ at $x_{i-\frac{1}{2}}$ is found through,

$$u^{\mathrm{R}}_{i-\frac{1}{2}} = \sum_{k=1}^{N+1} \omega_k u^{(k)}_{i-\frac{1}{2}}, \tag{B5a}$$

using,

$$u^{(1)}_{i-\frac{1}{2}} = \frac{1}{2}\bar{u}_{i-1} + \frac{1}{2}\bar{u}_i, \tag{B5b}$$

$$u^{(2)}_{i-\frac{1}{2}} = \frac{3}{2}\bar{u}_i - \frac{1}{2}\bar{u}_{i+1}, \tag{B5c}$$

and the linear weights,

$$\gamma_1 = \frac{1}{3}, \quad \gamma_2 = \frac{2}{3}. \tag{B6}$$

The reconstructed left state $u^{\mathrm{L}}_{i+\frac{1}{2}}$ at $x_{i+\frac{1}{2}}$ is found through,

$$u^{\mathrm{L}}_{i+\frac{1}{2}} = \sum_{k=1}^{N+1} \omega_k u^{(k)}_{i+\frac{1}{2}}, \tag{B7a}$$

using,

$$u^{(1)}_{i-\frac{1}{2}} = \frac{3}{2}\bar{u}_i - \frac{1}{2}\bar{u}_{i-1}, \tag{B7b}$$

$$u^{(2)}_{i-\frac{1}{2}} = \frac{1}{2}\bar{u}_i + \frac{1}{2}\bar{u}_{i+1}, \tag{B7c}$$

and linear weights,

$$\gamma_1 = \frac{2}{3}, \quad \gamma_2 = \frac{1}{3}. \tag{B8}$$

The smoothness indicators for both reconstructions at $u^{\mathrm{R}}_{i-\frac{1}{2}}$ and $u^{\mathrm{L}}_{i+\frac{1}{2}}$ are given by,

$$\beta_1 = (\bar{u}_i - \bar{u}_{i-1})^2, \tag{B9}$$

$$\beta_2 = (\bar{u}_{i+1} - \bar{u}_i)^2. \tag{B10}$$

B2 WENO5

The reconstructed right state $u^{\mathrm{R}}_{i-\frac{1}{2}}$ at $x_{i-\frac{1}{2}}$ is found through,

$$u^{\mathrm{R}}_{i-\frac{1}{2}} = \sum_{k=1}^{N+1} \omega_k u^{(k)}_{i-\frac{1}{2}}, \tag{B11a}$$

using,

$$u^{(1)}_{i-\frac{1}{2}} = \frac{11}{6}\bar{u}_i - \frac{7}{6}\bar{u}_{i+1} + \frac{1}{3}\bar{u}_{i+2}, \tag{B11b}$$

$$u^{(2)}_{i-\frac{1}{2}} = \frac{1}{3}\bar{u}_{i-1} + \frac{5}{6}\bar{u}_i - \frac{1}{6}\bar{u}_{i+1}, \tag{B11c}$$

$$u^{(3)}_{i-\frac{1}{2}} = -\frac{1}{6}\bar{u}_{i-2} + \frac{5}{6}\bar{u}_{i-1} - \frac{1}{3}\bar{u}_i, \tag{B11d}$$

and the linear weights,

$$\gamma_1 = \frac{1}{10}, \quad \gamma_2 = \frac{6}{10}, \quad \gamma_2 = \frac{3}{10}. \tag{B12}$$

The reconstructed left state $u^{\mathrm{L}}_{i+\frac{1}{2}}$ at $x_{i+\frac{1}{2}}$ is found through,

$$u^{\mathrm{L}}_{i+\frac{1}{2}} = \sum_{k=1}^{N+1} \omega_k u^{(k)}_{i+\frac{1}{2}}, \tag{B13a}$$

using,

$$u^{(1)}_{i-\frac{1}{2}} = -\frac{1}{6}\bar{u}_{i+2} + \frac{5}{6}\bar{u}_{i+1} + \frac{1}{3}\bar{u}_i, \tag{B13b}$$

$$u^{(2)}_{i-\frac{1}{2}} = \frac{1}{3}\bar{u}_{i+1} + \frac{5}{6}\bar{u}_i - \frac{1}{6}\bar{u}_{i-1}, \tag{B13c}$$

$$u^{(3)}_{i-\frac{1}{2}} = \frac{11}{6}\bar{u}_i - \frac{7}{6}\bar{u}_{i-1} + \frac{1}{3}\bar{u}_{i-2}, \tag{B13d}$$

and the linear weights,

$$\gamma_1 = \frac{3}{10}, \quad \gamma_2 = \frac{6}{10}, \quad \gamma_2 = \frac{1}{10}. \tag{B14}$$

The smoothness indicators for both reconstructions at $u^{\mathrm{R}}_{i-\frac{1}{2}}$ and $u^{\mathrm{L}}_{i+\frac{1}{2}}$ are given by,

$$\beta_1 = \frac{13}{12}\left(\bar{u}_i - 2\bar{u}_{i+1} + \bar{u}_{i+2}\right)^2 + \frac{1}{4}\left(3\bar{u}_i - 4\bar{u}_{i+1} + \bar{u}_{i+2}\right)^2, \tag{B15}$$

$$\beta_2 = \frac{13}{12}\left(\bar{u}_{i-1} - 2\bar{u}_i + \bar{u}_{i+1}\right)^2 + \frac{1}{4}\left(\bar{u}_{i-1} - \bar{u}_{i+1} + \right)^2, \tag{B16}$$

$$\beta_3 = \frac{13}{12}\left(\bar{u}_{i-2} - 2\bar{u}_{i-1} + \bar{u}_i\right)^2 + \frac{1}{4}\left(\bar{u}_{i-2} - 4\bar{u}_{i-1} + 3\bar{u}_i\right)^2. \tag{B17}$$

B3 WENO7

The reconstructed right state $u^{\mathrm{R}}_{i-\frac{1}{2}}$ at $x_{i-\frac{1}{2}}$ is found through,

$$u^{\mathrm{R}}_{i-\frac{1}{2}} = \sum_{k=1}^{N+1} \omega_k u^{(k)}_{i-\frac{1}{2}}, \tag{B18a}$$

using,

$$u^{(1)}_{i-\frac{1}{2}} = \frac{25}{12}\bar{u}_i - \frac{23}{12}\bar{u}_{i+1} + \frac{13}{12}\bar{u}_{i+2} - \frac{1}{4}\bar{u}_{i+3}, \tag{B18b}$$

$$u^{(2)}_{i-\frac{1}{2}} = \frac{1}{4}\bar{u}_{i-1} + \frac{13}{12}\bar{u}_i - \frac{5}{12}\bar{u}_{i+1} + \frac{1}{12}\bar{u}_{i+2}, \tag{B18c}$$

$$u^{(3)}_{i-\frac{1}{2}} = -\frac{1}{12}\bar{u}_{i-2} + \frac{7}{12}\bar{u}_{i-1} + \frac{7}{12}\bar{u}_i - \frac{1}{12}\bar{u}_{i+1}, \tag{B18d}$$

$$u^{(4)}_{i-\frac{1}{2}} = \frac{1}{12}\bar{u}_{i-3} - \frac{5}{12}\bar{u}_{i-2} + \frac{13}{12}\bar{u}_{i-1} + \frac{1}{4}\bar{u}_i, \tag{B18e}$$

and the linear weights,

$$\gamma_1 = \frac{1}{35}, \quad \gamma_2 = \frac{12}{35}, \quad \gamma_3 = \frac{18}{35}, \quad \gamma_4 = \frac{4}{35}. \tag{B19}$$

The reconstructed right state $u^{\mathrm{L}}_{i+\frac{1}{2}}$ at $x_{i+\frac{1}{2}}$ is found through,

$$u^{\mathrm{L}}_{i+\frac{1}{2}} = \sum_{k=1}^{N+1} \omega_k u^{(k)}_{i+\frac{1}{2}}, \tag{B20a}$$

using,

$$u^{(1)}_{i-\frac{1}{2}} = \frac{1}{12}\bar{u}_{i+3} - \frac{5}{12}\bar{u}_{i+2} + \frac{13}{12}\bar{u}_{i+1} + \frac{1}{4}\bar{u}_i, \tag{B20b}$$

$$u^{(2)}_{i-\frac{1}{2}} = -\frac{1}{12}\bar{u}_{i+2} + \frac{7}{12}\bar{u}_{i+1} + \frac{7}{12}\bar{u}_i - \frac{1}{12}\bar{u}_{i-1}, \tag{B20c}$$

$$u^{(3)}_{i-\frac{1}{2}} = \frac{1}{4}\bar{u}_{i+1} + \frac{13}{12}\bar{u}_i - \frac{5}{12}\bar{u}_{i-1} + \frac{1}{12}\bar{u}_{i-2}, \tag{B20d}$$

$$u^{(4)}_{i-\frac{1}{2}} = \frac{25}{12}\bar{u}_i - \frac{23}{12}\bar{u}_{i-1} + \frac{13}{12}\bar{u}_{i-2} - \frac{1}{4}\bar{u}_{i-3}, \tag{B20e}$$

and the linear weights,

$$\gamma_1 = \frac{4}{35}, \quad \gamma_2 = \frac{18}{35}, \quad \gamma_3 = \frac{12}{35}, \quad \gamma_4 = \frac{1}{35}. \tag{B21}$$

The smoothness indicators for both reconstructions at $u^{\mathrm{R}}_{i-\frac{1}{2}}$ and $u^{\mathrm{L}}_{i+\frac{1}{2}}$ are given by,

$$\begin{aligned}\beta_1 =& \bar{u}_i(2107\bar{u}_i - 9402\bar{u}_{i+1} + 7042\bar{u}_{i+2} - 1854\bar{u}_{i+3}) + \\ & \bar{u}_{i+1}(11003\bar{u}_{i+1} - 17246\bar{u}_{i+2} + 4642\bar{u}_{i+3}) + \\ & \bar{u}_{i+2}(7043\bar{u}_{i+2} - 3882\bar{u}_{i+3}) + \bar{u}_{i+3}(547\bar{u}_{i+3}),\end{aligned} \tag{B22}$$

$$\begin{aligned}\beta_2 =& \bar{u}_{i-1}(547\bar{u}_{i-1} - 2522\bar{u}_i + 1922\bar{u}_{i+1} - 494\bar{u}_{i+2}) + \\ & \bar{u}_i(3443\bar{u}_i - 5966\bar{u}_{i+1} + 1602\bar{u}_{i+2}) + \\ & \bar{u}_{i+1}(2843\bar{u}_{i+1} - 1642\bar{u}_{i+2}) + \bar{u}_{i+2}(267\bar{u}_{i+2}),\end{aligned} \tag{B23}$$

$$\begin{aligned}\beta_3 =& \bar{u}_{i-2}(267\bar{u}_{i-2} - 1642\bar{u}_{i-1} + 1602\bar{u}_i - 494\bar{u}_{i+1}) + \\ & \bar{u}_{i-1}(2843\bar{u}_{i-1} - 5966\bar{u}_i + 1922\bar{u}_{i+1}) + \\ & \bar{u}_i(3443\bar{u}_i - 2522\bar{u}_{i+1}) + \bar{u}_{i+1}(547\bar{u}_{i+1}),\end{aligned} \tag{B24}$$

$$\begin{aligned}\beta_4 =&\bar{u}_{i-3}(547\bar{u}_{i-3} - 3882\bar{u}_{i-2} + 4642\bar{u}_{i-1} - 1854\bar{u}_i)+\\ &\bar{u}_{i-2}(7043\bar{u}_{i-2} - 17246\bar{u}_{i-1} + 7042\bar{u}_i)+\\ &\bar{u}_{i-1}(11003\bar{u}_{i-1} - 9402\bar{u}_i) + \bar{u}_i(2107\bar{u}_i).\end{aligned} \tag{B25}$$

B4 Monotonocity Preserving Considerations

The monotonicity procedure presented by Balsara & Shu (2000) applied to the cell interface at $x_{i-\frac{1}{2}}$ is described, since the procedure at $x_{i+\frac{1}{2}}$ can be found in the original text to which the reader is referred for a more detailed description. The monotonicity procedure requires both the minmod and median functions

$$\text{minmod}(a_1, a_2, \ldots, a_n) = \frac{1}{n}\left[\sum_k^n \text{sign}(a_k)\right]\min\big(|a_1|, \ldots, |a_n|\big), \tag{B26a}$$

$$\text{median}(a, b, c) = a + \text{minmod}(b - a, c - a). \tag{B26b}$$

Curvature measures are then chosen using the cell averages defined in Eq. (B4),

$$d_i = u_{i+1} - 2u_i + u_{i-1}, \tag{B27}$$

which can used also to define the curvature at the zone boundary. A definition of the curvature at the cell interface is required such that smooth local extrema are not clipped which would result in a loss in the order of accuracy. Therefore, a limited curvature is defined from which the M4X strategy is adopted which offers the largest domain of support from those presented in the original literature,

$$d^{\text{M4X}}_{i-\frac{1}{2}} = \text{minmod}(4d_{i-1} - d_i, 4d_i - d_{i-1}, d_{i-1}, d_i, d_{i-2}, d_{i+1}). \tag{B28}$$

Maximum and minimum bounds $u^{R,\text{min}}_{i-\frac{1}{2}}$ and $u^{R,\text{max}}_{i-\frac{1}{2}}$, respectively, need to be found in which the solution $u^R_{i-\frac{1}{2}}$ must lie. The right-sided upper limit (UL) is found from

$$u^{\text{UL}}_{i-\frac{1}{2}} = u_i - \alpha(u_{i+1} - u_i), \tag{B29}$$

where in the present work $\alpha = 2$. The median (MD) is given by

$$u^{\text{MD}}_{i-\frac{1}{2}} = \frac{1}{2}(u_{i-1} - u_i) - \frac{1}{2}d^{\text{MD}}_{i-\frac{1}{2}}. \tag{B30}$$

Then the right-sided large curvature (LC) is given by

$$u^{\text{LC}}_{i-\frac{1}{2}} = u_i + \frac{1}{2}(u_i - u_{i+1}) + \frac{\beta}{3}d^{\text{LC}}_{i-\frac{1}{2}}, \tag{B31}$$

where in the present work $\beta = 4$. Finally, expressions for $u^{R,\text{min}}_{i-\frac{1}{2}}$ and $u^{R,\text{max}}_{i-\frac{1}{2}}$ are provided by

$$u^{R,\text{min}}_{i-\frac{1}{2}} = \max\left[\min\left(u_i, u_{i-1}, u^{\text{MD}}_{i-\frac{1}{2}}\right), \min\left(u_i, u^{\text{LC}}_{i-\frac{1}{2}}, u^{\text{UL}}_{i-\frac{1}{2}}\right)\right], \tag{B32}$$

$$u^{R,\text{max}}_{i-\frac{1}{2}} = \min\left[\max\left(u_i, u_{i-1}, u^{\text{MD}}_{i-\frac{1}{2}}\right), \max\left(u_i, u^{\text{LC}}_{i-\frac{1}{2}}, u^{\text{UL}}_{i-\frac{1}{2}}\right)\right], \tag{B33}$$

from which the montonicity preserving value of $u^R_{i-\frac{1}{2}}$ is finally obtained,

$$u^R_{i-\frac{1}{2}} = \text{median}\big(u^R_{i-\frac{1}{2}}, u^{R,\text{min}}_{i-\frac{1}{2}}, u^{R,\text{max}}_{i-\frac{1}{2}}\big). \tag{B34}$$

APPENDIX C: THIRD-ORDER TVD RUNGE–KUTTA METHOD

An explicit third-order TVD (Total Variation Diminishing) Runge–Kutta (RK3) method integrates the numerical solution in time. This can be summarized through the three stages,

$$\mathbf{U^{(1)}} = \mathbf{U^n} + \mathbf{\Delta t Q}(\mathbf{U^n}), \tag{C1a}$$

$$\mathbf{U^{(2)}} = \frac{1}{4}\left[3\mathbf{U^n} + \mathbf{U^{(1)}} + \mathbf{\Delta t Q}(\mathbf{U^{(1)}})\right], \tag{C1b}$$

$$\mathbf{U^{(3)}} = \frac{1}{3}\mathbf{U^n} + \frac{2}{3}\mathbf{U^{(2)}} + \frac{2}{3}\mathbf{\Delta t Q}(\mathbf{U^{(2)}}), \tag{C1c}$$

where Q denotes the numerical flux to be determined from the Riemann solver stage and $\mathbf{U}$ is the vector of conserved variables.

This paper has been typeset from a TEX/LATEX file prepared by the author.

On high-order numerical schemes for viscous relativistic hydrodynamics through the Kelvin–Helmholtz instability

Townsend, Jamie F.

2022-06-24

Townsend JF, Inutsuka S, Könözsy L, Jenkins KW. (2022) On high-order numerical schemes for viscous relativistic hydrodynamics through the Kelvin–Helmholtz instability, Monthly Notices of the Royal Astronomical Society, Volume 515, Issue 1, September 2022, pp. 451-472
https://doi.org/10.1093/mnras/stac1741